Additive Manufacturing 78 (2023) 103859

Contents lists available at ScienceDirect

Additive Manufacturing

journal homepage: www.elsevier.com/locate/addma

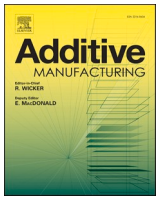

Evolution of microstructural heterogeneities in additively manufactured low-alloy steel

Ahmet Turnali [a,*], S. Amir H. Motaman [a], Yuling Chang [a], Bernd Böttger [b], Alexandros Serafeim [a], Lennart Sayk [c], Nicolas J. Peter [d], Silvia Richter [e], Alexander Schwedt [e], Simon Höges [f], Christian Haase [a]

[a] Steel Institute, RWTH Aachen University, 52072 Aachen, Germany
[b] Access e.V., 52072 Aachen, Germany
[c] Digital Additive Production, RWTH Aachen University, 52074 Aachen, Germany
[d] Institute of Energy and Climate Research (IEK-2), Forschungszentrum Jülich GmbH, 52425 Jülich, Germany
[e] Central Facility for Electron Microscopy, RWTH Aachen University, 52074 Aachen, Germany
[f] GKN Powder Metallurgy Engineering GmbH, 53177 Bonn, Germany

ARTICLE INFO

Keywords:
Additive manufacturing
Laser powder bed fusion
Low-alloy steel
Dual-phase steel
Microstructural heterogeneities

ABSTRACT

Understanding the complex phase transformations during additive manufacturing (AM) of low-alloy multi-phase steels is a necessary task to discover the mechanisms that lead to formation of AM-specific, heterogeneous microstructures. In the present study, investigations were carried out to gain fundamental insights on microstructure evolution of low-alloy steels during AM and upon post-AM heat-treatments. To this end, a low-alloy steel, with a composition similar to DP600 dual-phase (DP) steel, was processed by laser powder bed fusion (L-PBF). Subsequently, two post-L-PBF heat-treatments were applied to obtain ferritic-martensitic DP microstructures. The first heat-treatment consisted of austenitization followed by isothermal holding in ferrite (α)/austenite (γ) region (AIH), whereas the second comprised of inter-critical annealing (IC) in α/γ region. The as-built state exhibited a tempered martensitic microstructure with a weak (almost random) crystallographic texture in combination with compositional and morphological heterogeneities. Combination of multiphase-field simulation and multi-scale microstructure characterization revealed that the formation of compositional and morphological heterogeneities in as-built state was governed by consecutive liquid-solid (delta-ferrite (δ) → γ) and solid-solid (γ ↔ martensite (α′)) phase-transformations. For both post-L-PBF heat-treatments, Mn-segregation bands that formed during L-PBF led to heterogeneous α′ distribution after annealing. Electron microprobe analysis (EPMA) measurements revealed that the local Mn and C distributions were closely related to the spatial distribution of α and α′. The AIH heat-treatment resulted in annihilation of morphological heterogeneities, namely coarse- and fine-grained clusters. The absence of austenitization in IC heat-treatment resulted in distribution of ferritic-martensitic DP microstructure in coarse- and fine-grained clusters that inherited the L-PBF specific grain morphology distribution. Lastly, the IC state showed overall best mechanical properties due to the conservation of the heterogenous clustered microstructure, which potentially aided to simultaneously obtain high tensile strength (890.9 MPa) and relatively high ductility (20.5 %).

1. Introduction

Although the control of the geometrical aspects and the component design has advanced to a high level of maturity, the design, development, and optimization of the alloys explicitly profiting from the localized thermal histories offered by laser powder bed fusion (L-PBF) remains one of the biggest objectives for the materials science community [1]. During L-PBF, alloys experience a distinct thermal history associated with the iterative melting-solidification and heating-cooling cycles [2] accompanied with very high cooling rates [3] and temperature gradients [4]. These conditions result in complex liquid-solid and solid-solid phase transformations [5,6]. As such, the spatial change in thermal profiles facilitates the formation of locally varying microstructures that are heterogeneous on multiple length scales [7,8]. Microstructural heterogeneities formed during L-PBF often

* Corresponding author.
E-mail address: ahmet.turnali@iehk.rwth-aachen.de (A. Turnali).

https://doi.org/10.1016/j.addma.2023.103859

Available online 10 November 2023

Nomenclature

α	alpha-ferrite
γ	austenite
δ	delta-ferrite
α´	martensite
α´*	austenite grains with high dislocation density
$\varepsilon_{fracture}$	elongation at fracture
ω	grain major axis orientation
M_s	martensite start temperature
Ae_3	equilibrium austenitization temperature
Ae_1	equilibrium temperature at above which the formation of ferrite and austenite begins
G	thermal gradient
R	solidification velocity
AM	additive manufacturing
L-PBF	laser powder bed fusion
DP	dual-phase
DPLA	dual-phase low-alloyed
AIH	austenitization + isothermal holding
IC	inter-critical annealing
HAZ	heat affected zone
GND	geometrically necessary dislocation
PAGs	prior austenite grains
LAGBs	low angle grain boundaries
BD	building direction
SEM	scanning electron microscope
EBSD	electron backscatter diffraction
SE	secondary electron
LOM	light optical microscopy
EPMA	electron probe microanalysis
STEM	scanning transmission electron microscopy

comprise columnar grains with pronounced texture, heterogeneous grain sizes and morphologies, compositional heterogeneity, dislocation substructures, micro- and nano-precipitates depending on the processing parameters and alloy composition. Such hierarchically heterogeneous structures may reportedly promote unique material properties that, in some cases, cannot be achieved by their conventionally processed counterparts [6,7,9,10]. To exploit the materials design possibilities offered by L-PBF, a sound understanding of the evolution of heterogeneous microstructures and their related formation mechanisms is required [6,10–12].

In this context, implementing the characteristics of the L-PBF process can be utilized to re-design the microstructures of readily available multi-phase low-alloy steels, such as dual-phase (DP) steels, which are widely processed by conventional manufacturing routes, but so far hardly exploited by additive manufacturing (AM). Low-alloy steels are lean in chemical composition, hence, promote good weldability/processability and comparatively low raw-material cost [13,14]. The volume fraction, carbon content and morphology of the constituent phases can be altered by further heat treatments, offering another degree of freedom to manipulate the microstructure. Therefore, low-alloy steels are very flexible as their microstructure and mechanical properties can be widely tuned during AM processes and by post-AM heat-treatments [15]. Consequently, AM fabricated low-alloy steels can be utilized as geometrically complex structural parts where damage/energy absorption is required and offers a cheaper solution compared to its relatively expensive AM counterparts. Such possibilities make low-alloy steels an interesting candidate for a wide spectrum of AM applications in various industries.

Recently, several studies have addressed AM of low-alloy steels, yielding AM specific, heterogeneous microstructures. Dilip et. al. [16] processed a low-alloy martensitic HY100 steel using L-PBF. Repetitive heating and cooling cycles during L-PBF reportedly initiated the formation of heterogeneous microstructures consisting of tempered and untempered bands of martensite with a weak crystallographic texture. The as-built state exhibited higher yield and tensile strength compared to the traditionally processed counterparts. Seede et. al. [17] revealed the formation of weakly textured martensitic microstructure with alternating layers of martensite tempered in various degrees in a L-PBF fabricated ultra-high strength AF9628 low-alloy martensitic steel. The as-built state showed excellent tensile properties with up to 1.4 GPa tensile strength and 10.9 % fracture elongation, whereas the tensile properties were further improved by post-AM heat-treatments [18]. The as-built state (processed by directed energy deposition) of a DP steel fabricated by Sweet et. al. [15] exhibited a heterogeneous microstructure mainly comprised of fine-equiaxed ferrite as well as tempered martensite and bainite. The crystallographic texture was weak, and epitaxial growth during solidification was mostly absent. Upon post-AM heat treatments, ferritic-martensitic microstructures were obtained, and the tensile properties were comparable with conventional DP600.

The aforementioned studies on AM-fabricated low-alloy steels focused mainly on the relationship between processing by AM, microstructure and mechanical properties. However, the evolution of microstructural heterogeneities during L-PBF and post heat-treatments has not been quantified and studied systematically so far. On the one hand, understanding of L-PBF-induced liquid-solid as well as solid-solid phase transformations and their influence on the formation of microstructural heterogeneities in low-alloy steels is required. On the other hand, distinct thermal profiles inherent to L-PBF introduce the possibility to obtain L-PBF specific microstructures in as-built state. Nevertheless, a profound understanding of the underlying phase transformations is essential to actively make use of this possibility.

In the present study, we investigated the role of L-PBF-inherent characteristics and post heat-treatments on the underlying liquid-solid and solid-solid phase transformations and related microstructure evolution of a dual-phase low-alloyed (DPLA) steel. Multi-scale microstructure characterization was accompanied with multiphase-field simulation to gain fundamental insights into the phase transformation mechanisms and resultant microstructural heterogeneities. Furthermore, the influence of L-PBF-induced compositional and morphological heterogeneities on microstructure evolution and corresponding tensile properties of heat-treated states was critically discussed.

2. Material and methods

2.1. Material and processing

The commercially available DPLA powder (provided by GKN Powder Metallurgy Engineering GmbH, Germany) was used for AM utilizing the L-PBF technique. The cumulative size distribution of the powder at 10 % (D10), 50 % (D50) and 90 % (D90) was 17 μm, 33 μm and 56 μm, respectively. The chemical compositions of the powder and as-built bulk samples were measured by inductively coupled plasma optical emission

Table 1
Chemical composition (wt%) of the DPLA powder and as-built bulk specimens determined by ICP-OES analysis.

Elements [wt%]	Fe	C	Si	Mn	Ni, Cr, Cu	Mo
Powder	balance	0.11	0.18	1.73	<0.05	<0.005
120 W	balance	0.09	0.34	1.29	<0.05	<0.005
160 W	balance	0.08	0.36	1.25	<0.05	<0.005
200 W	balance	0.08	0.34	1.25	<0.05	<0.005

spectrometry (ICP-OES) and are summarized in Table 1**.** Mn evaporation and decarburization occurred during the L-PBF process. Bulk specimens for microstructural analysis and mechanical testing were fabricated using an Aconity-Mini L-PBF machine (Aconity-3D GmbH, Herzogenrath, Germany) equipped with a Yb:YAG fiber laser (400 W) with a Gaussian laser intensity profile and a focus diameter of 80 μm. The build chamber was purged with high purity Ar (purity $\geq$ 99.99 %) with a flow rate of 1 L/min to reach to chamber pressure of 50 mbar and an average oxygen concentration below 1 ppm. The L-PBF process parameters of layer thickness, hatch spacing, and laser scan speed were kept constant, whereas the laser power was varied according to Table 2. A rotation of 90° between subsequent layers and a bi-directional scanning strategy were applied. L-PBF parameters enabled the production of dense bulk materials (relative density $\geq$ 99.67 %), as acquired by optical residual porosity measurements of as-built cubic samples (**Fig. S1**). Micrographs for optical porosity measurements were taken using a Keyence VHX-600 digital microscope (Keyence GmbH, Germany) and post-image processing was conducted using the software ImageJ® [19].

Two post-L-PBF heat-treatment strategies were selected to obtain ferritic-martensitic dual-phase microstructures, namely austenitization and isothermal holding (AIH) and inter-critical annealing (IC), as schematically represented in Fig. 1**a**. In two-step AIH treatment, the austenitization was performed to alter the as-built microstructure similar to the homogenization process prior to inter-critical holding, whereas the one-step IC treatment was applied to utilize the as-built microstructure as a precursor for phase transformations during annealing. The AIH heat treatment consisted of annealing at 900 °C for 5 min to allow complete austenitization of the as-built microstructure, subsequent cooling to 700 °C and holding for 3 min in the ferrite (α)-austenite (γ) inter-critical region. During the IC heat treatment, the austenitization step was omitted and as-built samples were annealed in the α-γ inter-critical regime between the critical Ae_1 and Ae_3 temperatures at 800 °C for 20 min. After both heat-treatments, samples are water quenched below the M_s temperature to achieve γ to martensite (α´) transformation. The equilibrium phase diagrams were calculated using Thermo-Calc® software [20] 2020b release (Thermo-Calc Software, Sweden) in combination with TCFE10 Steels/Fe-alloys database for the nominal composition of the DPLA powder and of the as-built 120 W state (Fig. 1**b**). The equilibrium phase transformation temperatures and equilibrium γ contents at the respective inter-critical annealing temperatures of both states are given in Table 3**.** Influence of decarburization on equilibrium phase transformation temperatures and equilibrium γ contents was negligible. Therefore, carbon content is accepted as 0.09 wt% for thermodynamic calculations. In the following, the as-built samples will be denominated with respect to the applied input laser power (e.g., as-built 120 W) and heat-treated samples with respect to the heat-treatment strategy – laser power (e.g., AIH - 120 W).

2.2. Microstructure and mechanical characterization techniques

Cubic samples for microstructure analysis were manufactured by L-PBF with dimensions of 10 × 5 × 5 mm^3. Microstructure analysis was performed on the cross-sections of the samples in direction parallel to the building direction (BD). The samples were prepared by mechanical grinding up to 2500 SiC grit paper, mechanical polishing with 6 and 1 μm diamond suspension, and subsequent etching using a 3 % Nital solution (3 wt% HNO_3, 97 wt% ethanol). Various imaging techniques were utilized including light optical microscopy (LOM) and scanning electron microscopy (SEM) using secondary electron (SE) imaging, in-lens imaging and electron backscatter diffraction (EBSD). SEM and EBSD measurements were performed on a Zeiss Sigma field emission gun (FEG) SEM with EBSD and EDS detectors (Oxford Instruments plc, Great Britain). SE and in-lens micrographs were taken at an accelerating voltage of 20 kV with a working distance between 8 and 9 mm and an aperture size of 75 μm. For EBSD analysis, mechanically polished samples were further electropolished at 22 V for 10 s at room temperature using a LectroPol-5 electrolytic polishing machine (Steuers GmbH, Germany) and an A2 electrolyte (Steuers GmbH, Germany). EBSD measurements were conducted with an accelerating voltage of 20 kV, a working distance between 14 and 16 mm and a step size of 200 nm on a cubic grid. Noise reduction and analysis of the EBSD data was carried out via the MATLAB-based (Mathworks Inc., USA) toolbox MTEX [21–23]. Prior austenite grain (PAG) reconstruction was performed in MTEX by using the add-on function library ORTools [24].

Table 2
L-PBF process parameters for the production of bulk specimens.

Laser power[W]	Laser scan speed[mm/s]	Hatch spacing[μm]	Layer thickness[μm]	Focus diameter[μm]
120	550	60	30	80
160	550	60	30	80
200	550	60	30	80

Electron probe microanalysis (EPMA) elemental mappings were acquired by an electron microprobe device (JEOL JXA-8530 F Ltd., Tokyo, Japan) with an acceleration voltage of 15 kV and a beam current of 400 nA, and a step size of 200 nm with a dwell time of 40 ms was used for the mappings to cover larger areas. EPMA line scans were performed by moving the electron beam with a step size of 50–200 nm and dwell time of 5 s. The complementary EBSD measurements to the EPMA maps were performed with an accelerating voltage of 15 kV, a working distance of 15 mm, and a step size of 50 nm by using Zeiss GeminiSEM 300 with a Symmetry EBSD detector (Oxford Instruments plc, Great Britain).

Samples for scanning transmission electron microscopy (STEM) were prepared using a dual beam Helios NanoLab400S (ThermoFischer Scientific, formerly FEI, Netherlands) focused ion beam (FIB). STEM lamellae were prepared from the center of the cubic specimens in cross-section parallel to BD. A conventional lift-out technique was applied to transfer the thick STEM lamella onto a STEM grid. Finally, the STEM samples were thinned down to electron transparency with a final thinning step consisting of 5 kV ion polishing to reduce beam damage and Ga contamination as much as possible. Scanning transmission electron microscopy (STEM) was carried out at 200 kV and with a semi-convergence angle of 24.7 mrad in an aberration-corrected Titan G^2 60–200 CREWLEY microscope (ThermoFischer Scientific, formerly FEI, Netherlands) equipped with a high-brightness field emission electron gun and a Super-X energy-dispersive X-ray spectroscopy (EDS) system. Low-angle annular dark-field (LAADF) images were acquired to make use of the associated strain contrast with a semi-collection angle of 31–187 mrad.

For determination of tensile properties, standing cylindrical specimens were manufactured parallel to the building direction. As-built and heat-treated cylinders were machined to B4×20 tensile specimens according to DIN 50125 (**Fig. S2**). Quasi-static uniaxial tensile tests were performed at room temperature on a Z100 (Zwick/Roell GmbH & Co. KG, Germany) at a constant strain rate of 0.001 s^{-1} until fracture. Two to three specimens were tested for each condition, and average values are represented. Vickers microhardness measurements were conducted using a ZHμ microhardness tester (Zwick/Roell GmbH & Co. KG, Germany) with 100 g load and 10 s dwell time on the samples used for microstructure analysis. At least three indentations per respective area were performed.

2.3. Modelling the evolution of solidification microstructure of DPLA steel under L-PBF conditions

The phase-field method enables the simulation of microstructure evolution in multi-component systems over time and space during phase transformations. These simulations are fundamentally governed by thermodynamic driving forces, interfacial curvature, and diffusion. A detailed description of the phase-field model can be found in the **Appendix** based on the references [25,26]. It has been previously shown

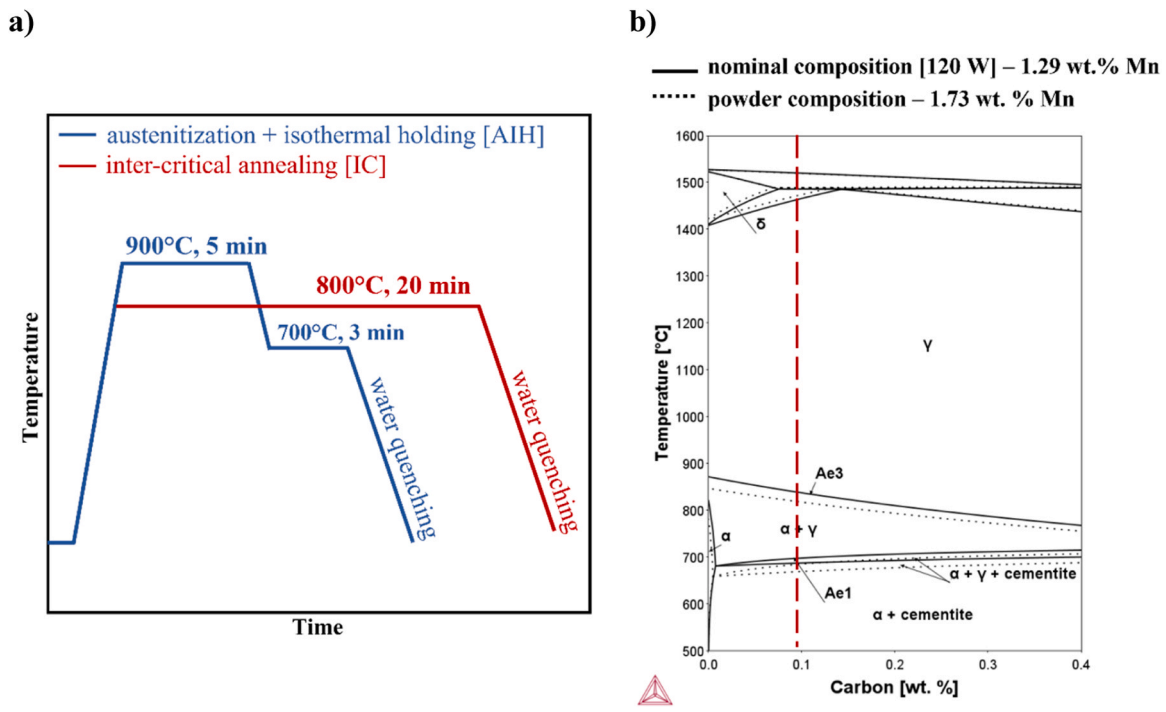

Fig. 1. (a) Post heat-treatment strategies and (b) calculated equilibrium phase diagram based on the nominal compositions of the as-built 120 W state (black straight lines) and of the DPLA powder (black dashed lines). The red dashed line indicates the C content.

Table 3
Comparison of equilibrium phase transformation temperatures and equilibrium γ (austenite) contents at different temperatures for as-built 120 W sample and DPLA powder based on the difference in Mn contents.

Mn content [wt%]	Ae_1 [°C]	Ae_3 [°C]	γ at 700 °C [vol%]	γ at 800 °C [vol%]
1.29 [120 W]	696.8	840.6	13.8	50.4
1.73 [Powder]	686.7	814.7	20.7	78.8

that by using phase-field models, a decent quantitative agreement with experiments can be achieved under thermal profiles resembling the L-PBF conditions [27–29]. In the present study, multiphase-field simulations of the microstructure evolution of the DPLA steel under L-PBF conditions were performed based on the multiphase-field approach [25,26], using the phase-field solver MICRESS® (version 7.100, ACCESS e. V., Germany). The aim of the simulations was to reveal the phase transformation mechanisms at higher temperatures, i.e., liquid-solid and solid-solid phase-transformations during the single pass. The discretized (in building direction) time-dependent 1D-temperature profiles for the simulation domain were acquired from single-track melt pool simulations using the finite-element (FE) solver ABAQUS (Dassault Systèmes SE, France) which are based on an experimentally validated FE model introduced for L-PBF in [30]. The input parameters for the FE-simulation such as the liquidus ($T_{Liquidus}$ = 1520.48 °C) and solidus ($T_{Solidus}$ = 1486 °C) temperatures, latent heat and temperature dependent material properties (i.e., specific heat capacity and density) were calculated based on the nominal composition of the as-built 120 W state (Table 1) by using the Thermo-Calc® [20] TCFE10 Steel/Fe-alloys database. The model setup, simulated melt pool cross-section, corresponding temperature profile and cooling rates are presented in Fig. 2. The multiphase-field simulations were performed in 2D with a 15 nm grid spacing, and the simulation domain was implemented as 30 μm x 60 μm (in building direction) in order to represent the center area of the melt pool cross-section. An initial microstructure at t = 0 was defined as an almost flat solid-liquid interface, whereas the solid grains represented a portion of previously deposited layers. Since metastable phase transformations, such as reverse or forward γ ↔ α′ transformation, cannot be selected from the thermodynamic database, the re-austenitization behavior of α′ in previously deposited layers was emulated by description as γ-grains with high initial dislocation densities ranging from 5.0E+14 to 2.0E+15 m^{-2}. The range of dislocation densities was selected from the geometrically necessary dislocation (GND) densities obtained by post-processing of the EBSD data with the MATLAB-based toolbox MTEX following the approach introduced in [31]. The γ-grains with high initial dislocation density are denoted as α′* in the following text. The initial compositions for both solid and liquid were defined as the nominal composition of the as-built 120 W state. For simplicity, only the nominal contents of Fe, Mn, Si and C were considered. The solid (α′*) grains inherited the C and Mn partitioning from deposition of the previous layer to represent local phase stabilities and transformation kinetics carefully. The previously deposited α′*-grains was acquired by performing a precursor simulation (using identical 1D-temperature profile) that underwent liquid → δ → γ transformation in order to implement the solidification and solid-solid phase transformation related Mn and C partitioning in initial microstructure. In the beginning of the simulation, the domain was heated from top by applying the time-dependent temperature profiles from the ABAQUS simulation, thus initiating the melting of the pre-existing α′* layer as well as its partial transformation to γ in the heat affected zone (HAZ), hence, emulating the re-melting and re-austenitization, and the solidification behavior during L-PBF. During the multiphase-field simulation, nucleation of delta-ferrite (δ) was initiated at the γ-liquid interface, whereas nucleation of γ was allowed at δ-liquid, δ-δ interfaces, δ triple junctions and α′*/ α′* interfaces. A fixed orientation relationship between δ and γ during δ to γ transformation enabled to mimic a parent/child relation between bcc and fcc. The maximum nucleation temperature for both δ and γ was selected as $T_{Liquidus}$ in order to ensure a competitive phase selection between δ and γ during solidification. The interfacial energies corresponding to liquid/ δ, liquid/γ, δ/γ and α′*/α′* were selected as 2.04E-5, 3.19E-5, 3.7E-5 [32], and 2.0E-5 J/cm^2 [33], respectively. In order to allow realistic interpretation of temperature-dependent thermodynamic driving forces and diffusion, the simulation was coupled

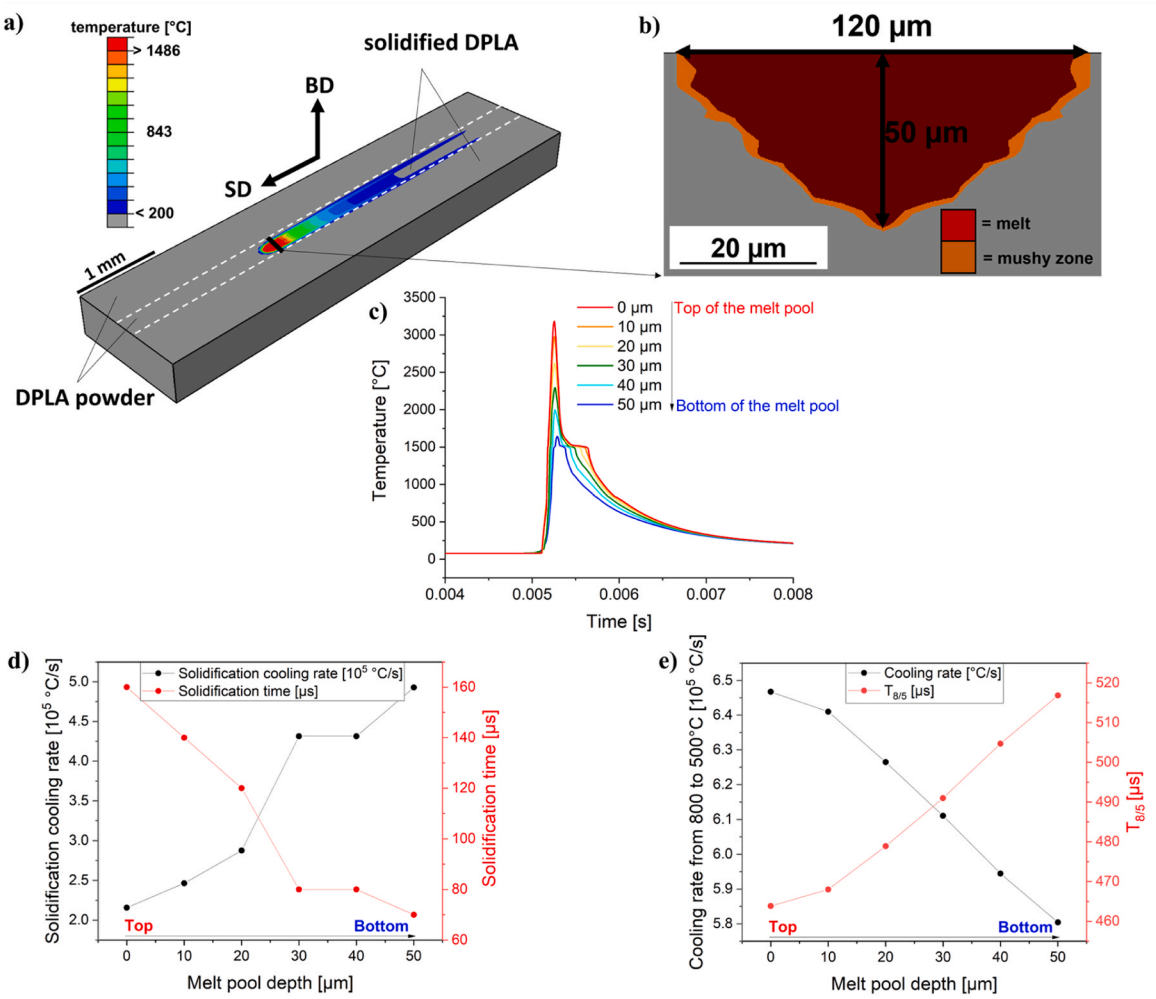

Fig. 2. Single-track simulation of the as-built 120 W state using a FE-model, as described in [30]. The building and scanning directions are depicted as BD and SD, respectively. (a) Simulation setup displaying transient temperature profiles and melt pool geometries during solidification under selected L-PBF condition, (b) the respective cross-section of the simulated melt pool, (c) temporal temperature evolution of selected nodes from the cross-section presented in (b), (d) solidification cooling rate and solidification time between $T_{Liquidus}$ and $T_{Solidus}$ as a function of the melt pool depth, (e) cooling rate and cooling time between 800 and 500 °C as a function of the melt pool depth. 50 µm represents the bottom boundary of the melt pool, whereas 0 µm depicts the top of the melt pool. Nodes were selected with 10 µm increments.

with the thermodynamic and mobility databases TCFE10 and MOBFE4 from Thermo-Calc®. Redistribution of the elements at the fast moving solid-liquid interfaces was calculated including an anti-trapping current [34], and automatic mobility correction was used in MICRESS® to correct for numerical trapping effects of the diffuse interface and to assure diffusion-limited interface kinetics.

3. Results and discussion

3.1. Phase transformation mechanisms during L-PBF

Fig. 3 shows the micrographs of the cross-sections of the as-built 120 W sample parallel to the building direction (BD). The location of the micrographs with respect to the overall cross-section parallel to BD were shown in **Fig. S3a** whereas the single hardness line trace (HV1) with low hardness deviation (~3.7 %) along the BD was presented in **Fig. S3b** in order to provide a rationale for location of microstructure characterization in middle layers. The hardness (HV0.1) values of individual indentations in Fig. 3 were also shown in **Fig. S4**. A clear difference in microstructural features was observed between the topmost and middle layers of the as-built state (Fig. 3**a-b**). Since the topmost layer has not experienced re-melting, re-heating and re-cooling effects from above deposited layers, it provides a solid basis to understand the microstructure evolution during the initial solidification. Lath-shaped martensite (α′) was revealed in the topmost layer (Fig. 3**b**), as typically observed in low and medium carbon steels due to higher α′ transformation temperatures [13].

In contrast to the top layer, the middle layers were heat-affected, as they underwent re-heating and re-cooling cycles during the deposition of subsequent layers. The as-built 120 W sample displayed curved melt pool morphology with distinct dark and bright HAZ, as shown in the optical micrographs in Fig. 3**a**. The darker boundaries in the middle layers depict the vicinity of the prior melt pool boundaries, whereas the brighter areas are the prior melt pools. The microstructure of the middle layers in the as-built 120 W sample was characterized in detail by SEM and STEM, as shown in Fig. 3**b** and Fig. 4, respectively. The middle layers exhibited heterogeneous grain morphologies along the HAZ. Columnar grains grew from the prior melt pool boundaries and emerged toward the center of the melt pool (e.g., direction of maximum heat extraction), whereas the region in the vicinity of the prior melt pool boundaries showed finer grains. The morphologically identical orientation of laths is visible in the α′-blocks (Fig. 3**b**) together with the dislocation networks in the α′-substructure (Fig. 4), indicating that α′ is globally present in the as-built state. Similar observations for topmost

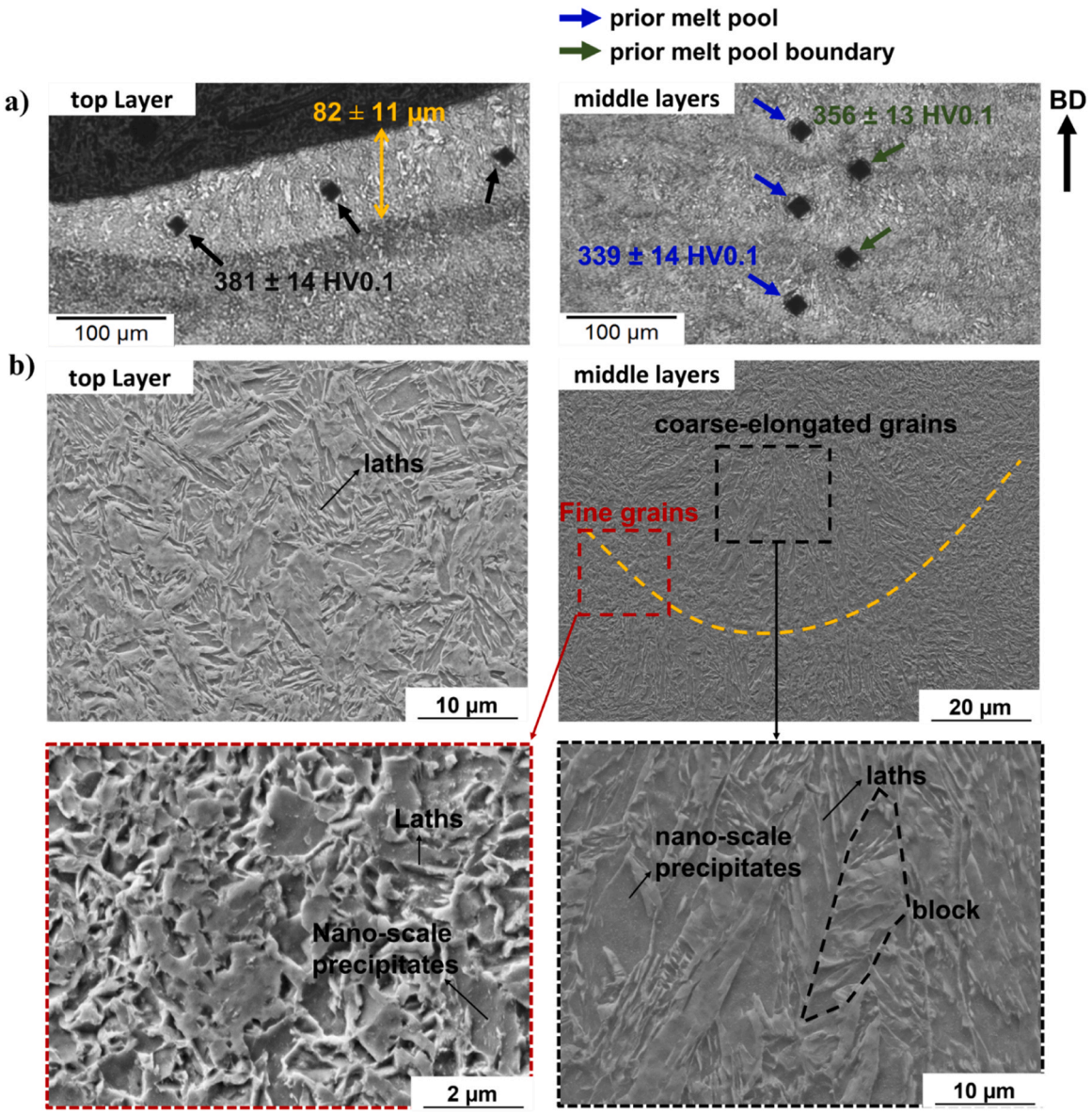

Fig. 3. Microstructure characterization of the as-built 120 W state obtained parallel to the BD. (a) Optical micrographs and (b) SE micrographs of etched cross-sections from topmost and middle layers of the bulk specimen. Indents indicate the locations of the microhardness measurements. The orange dashed line indicates a prior melt pool boundary in the micrograph taken from the middle layers in (b).

and middle layers are visible for as-built 160 and 200 W samples (**Figs. S5** and **S6**), indicating that an increase in energy input and corresponding re-heating and re-cooling cycles during L-PBF process resulted in a microstructure that mainly consist of α′ with coarser grains compared to as-built 120 W sample (**Figs. S7 and S8**).

To reveal the liquid-solid and solid-solid phase transformation mechanisms at higher temperatures during L-PBF, multiphase-field simulations were performed. Phase distributions, phase and inverse pole figure (IPF) orientation maps of reconstructed prior austenite grains (PAGs) from the EBSD data, and elemental distributions were represented in Fig. 5.

At initial state (t = 0, Fig. 5**a**), the simulation domain represents the cross-section where α′* grains (austenite (γ) grains with high initial dislocation densities and elemental partitioning) and already molten DPLA powder co-exist. In order to emulate the re-melting, re-austenitization, and solidification during the L-PBF process, the simulation started with partial re-melting of the previously deposited layer. At t = 11 µs, re-melting of α′* was complete, and the simulation domain represents the partially re-melted α′* layer and the melt pool boundary (fusion line) as shown with black dashed lines. In the following, the formation of primary delta-ferrite (δ) was observed by heterogeneous nucleation on partially re-melted α′* grains. Meanwhile, nucleation of new γ grains was initiated on α′*/α′* interfaces in previously deposited layers (below the melt pool boundary). As the solidification proceeded, the γ stabilizing elements C and Mn were continuously rejected from solidifying δ and enriched in the remaining liquid melt (Fig. 5**b**), whereas the temperature decreased in the solidified portion underneath. Consequently, the temperature for γ formation was reached, leading to nucleation and growth of γ at C and Mn enriched locations (e.g., at δ /δ boundaries and triple junctions at t = 100 µs in Fig. 5**a**). At t = 250 µs, the solidification proceeded as primary δ, and γ formation solely took place by solid-state transformation, eventually leading to complete transformation of the remaining δ into γ-grains with low angle grain boundaries (LAGBs) that retain the elongated grain shape (in building direction) due to their nucleation with an orientation relationship to the δ-grains (t = final). Meanwhile, re-austenitization of previously deposited layers persisted, where fresh γ-grains below the melt pool boundary continued to grow into parent grains and eventually formed the region

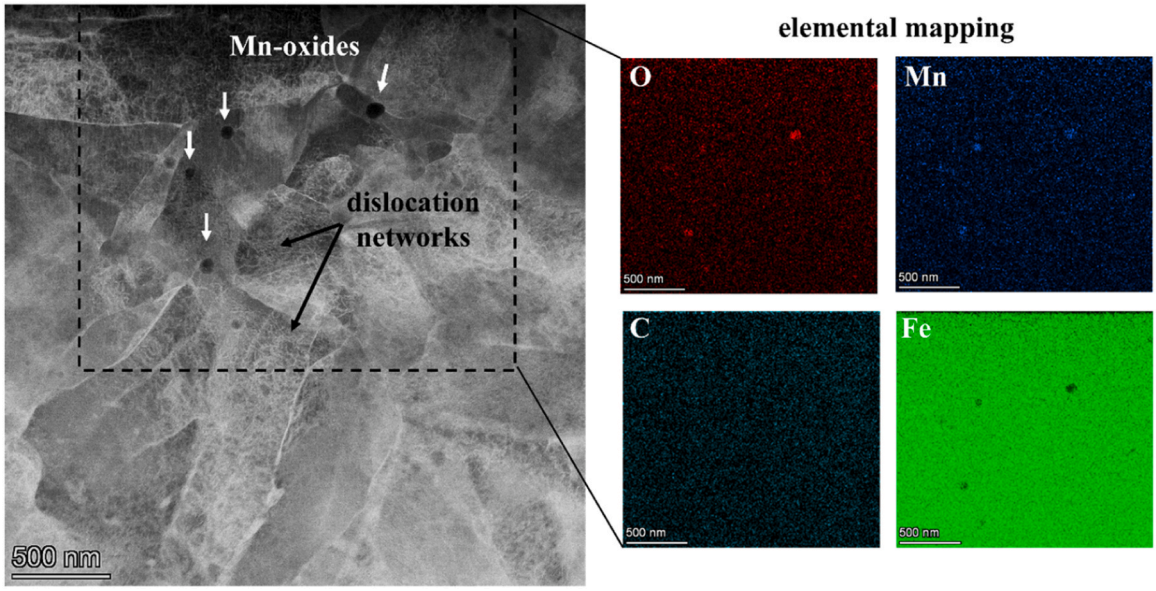

Fig. 4. STEM-LAADF image and respective EDS elemental mappings of Fe, Mn, C and O acquired from the middle-layers of the as-built 120 W state.

exclusively consisting of fine γ-grains with random orientations as seen in phase and IPF maps of PAGs in Fig. 5**a**. Moreover, multiphase-field simulations revealed that Mn partitioning was mainly governed by δ solidification, whereas C partitioning was determined by chronological orders of δ solidification and δ → γ transformation in solid-state. C was initially rejected from δ and enriched in inter-dendritic regions during δ solidification, leading to C-depletion in the δ-dendrite cores. After γ transformation, C was enriched in γ-grains, showing a positive correlation with Mn-enriched regions, whereas the C content was lower in the regions closer to γ-interfaces/boundaries, as can be seen from the virtual EDX line scans acquired from the condition at t = 100 μs (Fig. 5**b**).

The multiphase-field simulations provided significant insights into the evolution of the as-built microstructure. The results clearly revealed that the phase transformations during L-PBF occurred in multiple steps, i.e., δ solidification was followed by complete transformation into γ by nucleation and growth in solid-state. Since metastable phases, such as α′, cannot be selected from thermodynamic databases, the current multiphase-field model was not eligible to investigate the γ → α′ transformation during subsequent cooling. Therefore, cooling rates were extracted from FE-simulations for the temperature range between 800 and 500 °C, where the critical phase transformations occur in steels (e.g., bainitic and martensitic transformations), to validate α′ formation in the as-built microstructure. According to the FE-simulations, the cooling rate between 800 and 500 °C was in the range of 6×10^5 K/s (Fig. 2**e**), which was well above the critical cooling rate for α′ formation in dual-phase steels [35–37]. Therefore, the γ further transformed into α′ (as morphologically visible in Fig. 3) during subsequent cooling because of the rapid cooling rates associated with the L-PBF process.

Subsequent to the α′ formation, the fresh α′ was in-situ heat-treated, as it was exposed to re-heating cycles along the progressive deposition of adjacent layers together with the heat-accumulation within the solidified material [38]. The regions closer to the melt pool experienced higher temperatures above the complete austenitization (Ae_3) temperature. Consequently, some fraction of existing α′ initially transforms into γ during re-heating (Fig. 5**a**) and transforms back to α′ during cooling as the laser source continued to move. The regions distant from the melt pool could be exposed to temperatures below the austenitization (Ae_1) temperature. Such regions underwent in-situ tempering [39]. Dilip et. al. [16] and Seede et. al. [17] observed in-situ tempered and austenitized zones in low-alloy martensitic steels produced by L-PBF. Dilip et. al [16] suggested that the in-situ tempering effect leads to softening of existing α′ and precipitation of nano-scale carbides within α′ owing to the diffusion of carbon from supersaturated α′. In the present study, a distinct drop in microhardness values was observed upon transition from topmost to the middle layers as shown in Fig. 3**a**. The highest hardness values measured in the top layer (381 ± 14 HV0.1) are consistent with the formation of a fresh martensitic microstructure (Fig. 3**a-b**) that did not undergo re-heating and cooling cycles from the above deposited layers, and as a consequence, did not experience tempering [16]. Along the HAZ, the prior melt pools exhibited slightly lower hardness (339 ± 14 HV0.1) compared to the regions associated with the prior melt pool boundaries (356 ± 13 HV0.1). Overall, the results suggested that the middle layers were characterized by significantly lower microhardness values compared to the topmost layer. Therefore, initially re-austenitized regions were also subjected to temperatures below the onset austenitization temperature (Ae_1), facilitating in-situ tempering of α′ throughout the HAZ [38]. According to SE micrographs (Fig. 3**b**), the investigated as-built state showed nano-scale precipitates in the HAZ independent from the temporal evolution of the temperature profiles in various distances to the melt pool. In order to understand the nature of the nano-scale precipitates, elemental mappings were performed as shown in Fig. 4. The nano-scale precipitates were identified as Mn-oxides that were dispersed in the martensitic matrix. During L-PBF, the high-power laser facilitates the dissolution of oxides that are already present in the powders into the melt. Subsequently, oxide particles can precipitate into ultrafine dispersions along the rapid-solidification since the cooling rates (~10^6 K/s) within the oxide-formation temperature range falls into the range of cooling rates typically observed during L-PBF [40].

To investigate the local element distributions, qualitative concentration maps and quantitative line-scans of Mn and C of the as-built and heat-treated 120 W samples were obtained by EPMA measurements, as demonstrated in Fig. 6. It should be noted that some remaining contamination is visible at the boundary of the carbon intensity maps due to a longer stay of the beam during the scanning procedure. The EPMA measurements were complimented with EBSD band slope analysis, which measures the sharpness of the Kikuchi diffraction pattern, to show the related differentiation between the EBSD pattern quality of the bcc products, such as α, α′ and tempered α′. Since α′ induces lattice defects upon its transformation, it can be distinguished by lower band slope values [41]. The EPMA maps of the as-built 120 W state revealed that Mn was mainly enriched in the vicinity of prior melt pool

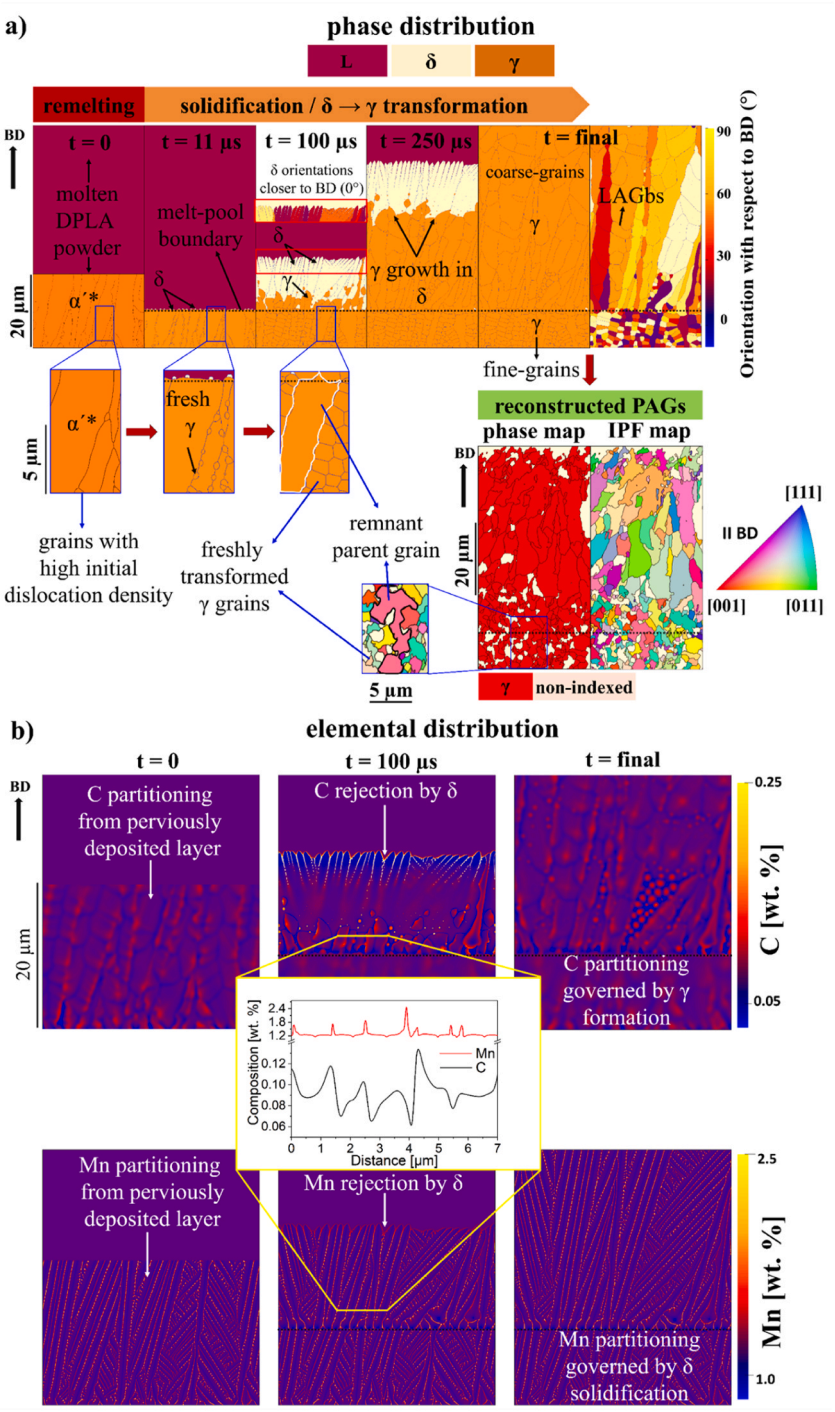

Fig. 5. Multiphase-field simulation results for remelting, re-austenitization and solidification of the as-built 120 W state under L-PBF conditions. The simulation domain represents the center of the melt pool cross-section (until selected heights) paralell to BD. The austenite grains with initially high dislocation densities are represented as α´*. Black dashed lines represent melt pool boundaries. (a) Microstructure evolution and its comparison with experimental EBSD phase and IPF orientation maps of reconstructed PAGs (see also overview in **Fig. S7**). Grain orientations are given in degrees (°), where BD is 0°. (b) C and Mn distributions at given time steps. Yellow lines show the locations of virtual EDX taken at t = 100 µs.

boundaries, whereas C partitioning in tempered α´ was revealed by the fine line- and island-shaped patterns of high C concentration. Moreover, EPMA line-scans further displayed the Mn and C partitioning along the α´-grains, where the positive correlation between Mn and C composition can be clearly seen (Fig. 6**d**).

The origin of the Mn enrichment in the vicinity of the prior melt pool boundaries can be related to the sudden increase in solidification velocity (R) towards the center of the melt-pool. Relatively stronger Mn rejection takes place into the liquid during instationary solidification of δ, with higher thermal gradient (G) and lower R compared to the center and top of the melt pool. This phenomenon causes more solute (Mn) to be rejected into the liquid at the solid/liquid interface, leading to an increase in Mn content in the remaining melt. Accordingly, the material that solidifies right after the increase in R possesses higher Mn content

[39], visible as Mn-bands in Fig. 6. During the subsequent cooling and heating cycles, the low diffusivity of Mn in the solid phases retained the solidification-related compositional patterns governed by δ solidification (i.e., Mn-bands and micro-segregation), as also revealed by the multiphase-field simulations (Fig. 5). However, due to the much higher diffusivity of interstitial elements in the solid, the C distribution during L-PBF was mainly determined by the C-solubility in each phase along the consecutive liquid-solid and solid-solid phase transformations. According to the multiphase-field simulations (Fig. 5), C was initially rejected to inter-dendritic regions during δ solidification. After δ to γ transformation, C-enrichment was found surrounding the micro-segregation patterns of Mn, as displayed by the virtual EDX line scans given for t = 100 μs (Fig. 5**b**). Therefore, in the areas where γ stability was locally higher (such as Mn enriched regions), γ can form easier owing to the lower Ae_1 and Ae_3 temperatures (Fig. 1**b** and Table 3) and act as preferred locations for further C enrichment due to the locally higher C solubility. Upon martensitic transformation, i.e., during cooling down below the martensite start (M_s) temperature, a complete suppression of C-diffusion was not possible owing to the high M_s temperature (411 °C) of the investigated low-alloy steel [42]. Hence, it can be concluded that C-diffusion continued during α´ transformation towards lath-, interface-boundaries and locations with high Mn-partitioning, resulting in fine line- and island-shaped C-partitioning, as verified in the EPMA maps and line scans (Fig. 6**c** and **d**).

3.2. Evolution and quantification of morphological heterogeneities in as-built state

The microstructure of the as-built 120 W state was characterized by EBSD in terms of crystallographic orientation and grain morphology distributions. Fig. 7 displays the representative EBSD images taken from the center of the cubic cross-sections along BD. The grain morphological descriptors associated with the grain size and shape are summarized in **Table S1**.

EBSD inverse pole figure (IPF) orientation maps and IPF plots are shown in Fig. 7**a.** In as-built 120 W state, the IPFs revealed that the martensitic microstructure had a weak (almost random) texture corresponding to <111>|| BD with a maximum intensity of 1.4. Based on the EBSD analysis, a very small amount of γ (fraction <0.1 %) was observed in as-built state (**Fig. S9**).

According to the multiphase-field simulation (Fig. 5**a**), the orientations of the majority of the δ solidification grains are well aligned (<30°) with the building direction (i.e., almost parallel to BD, direction of highest temperature gradient) at t = 100 μs, whereas the orientation of γ-grains strongly deviated from the parallel alignment with respect to the BD (0°) at t = final. Hence, the simulation results suggest that the δ-grains that solidified along the direction of maximum heat extraction had disappeared (Fig. 5**a**) as a result of solid-state phase transformation that was governed initially by means of δ → γ. Considering that solid-state phase transformations also occurred during re-heating and re-cooling cycles in terms of re-austenitization and subsequent γ → α´ transformation, the variance in orientations can be selected with respect to the orientation relationships between δ → γ and γ → α´ [43], which eventually ensued weakening of the crystallographic texture, as shown in Fig. 7**a**.

The microstructure of the as-built 120 W state exhibits morphological heterogeneities associated with the emergence of distinct coarse- and fine-grained clusters, as depicted in Fig. 7. The coarse-grained (area fraction of 0.46) and fine-grained (area fraction of 0.54) clusters were distinguished primarily based on the size of their constituent grains. The number of contiguous neighbors has been considered as an auxiliary criterion to divide the microstructure into the two cluster species. The grain morphology of the as-built state was carefully analyzed using various morphological descriptors (**Table S1**), such as grain size (Fig. 7**b**), grain aspect ratio (Fig. 7**c**) and grain anisotropy index (Fig. 7**d**) to quantitatively evaluate the effect of AIH and IC heat-treatments on the evolution of the morphological heterogeneities (Section 3.3). According to the analysis, the nominal effective grain size of the as-built 120 W state was 2.2 μm, while it was 2.9 μm (+24.1 %) in the coarse-grained clusters and 1.66 μm (−32.5 %) in the fine-grained clusters, indicating that the effective grain size was about two times larger in coarse-grained clusters compared to their fine-grained counterparts. The mild deviation in the effective aspect ratio of coarse-grained clusters by −5.5 % and fine-grained clusters by + 3.7 % from the nominal mean value of 0.54 revealed the elongated grain morphology. As another grain shape descriptor, the average grain shape anisotropy index in the coarse- and fine-grained clusters, were 48 % and 33 %, respectively (Fig. 7**b**). The grain shape anisotropy index is defined as a measure for the degree of deviation of an arbitrarily shaped grain from its equivalent circle/sphere (equiaxed shape) [44,45]. Thus, when transitioning from fine- to coarse-grained clusters, more pronounced deviation from the equiaxed shape was observed.

From the grain orientation (t = final) and reconstructed PAG maps in Fig. 5**a** and SE micrographs in Fig. 3**b,** fine grains were observed to be mainly concentrated at the bottom of the melt pool, whereas the rest of the melt pool comprised mainly of coarse-elongated PAGs. In addition, the heterogeneity of grain morphologies was also displayed at the meso-structure level, where the emergence of irregular clusters of coarse and fine grains was revealed by EBSD analysis in Fig. 7. From the multiphase-field simulations (Fig. 5), different formation mechanisms can be suggested for coarse and fine grains, respectively. Firstly, the formation of relatively coarse-elongated γ-grains appeared to originate from their growth started at the interfaces of the δ-grains. Initial δ-solidification and subsequent γ-formation in solid-state were previously reported in welding literature for low-alloy steels with similar compositions [46–48]. Owing to the high temperature gradients, δ-grains are expected to solidify in dendritic or cellular shape towards the direction of maximum heat-extraction, leading to columnar morphologies. Upon subsequent cooling, γ-nucleation at δ-boundaries takes place, and growth of γ at δ-boundaries results in the formation of columnar γ-grain morphologies, which closely represent former δ-grain morphology [46], i.e., the major axes of newly formed γ-grains were well aligned with the direction of maximum heat extraction. It has been argued that upon the decomposition of δ, newly formed γ can preferably grow along the δ sub-boundaries and/or interphase boundaries as a result of enhanced diffusion along the interfaces [49,50]. As can be seen from EBSD orientation maps for reconstructed PAGs and as-built state in Fig. 5 and Fig. 7, respectively, the investigated melt pools indeed exhibited elongated grains and their grain major axes followed the direction of maximum heat flow. However, the crystallographic orientation distribution did not show a strong allocation (i.e., <100> || BD) but it was rather almost random. This finding clearly demonstrates that the γ phase was not the primary phase to be formed during solidification. Instead, γ must have nucleated afterwards at δ-grain boundaries. The hypothesis of γ-grains reaching columnar shape by growing along the δ-grain boundaries would require them to nucleate and grow rapidly enough despite random orientation. Such a behavior could not be achieved by multiphase-field simulations but also cannot be rigorously excluded. Instead, δ-to-γ transformation was described by nucleation of γ at δ-grain boundaries with parent orientation relationship. Accordingly, the δ-grains were replaced by multiple γ-grains that were separated by LAGBs. Thus, our experimental observations strongly supported the outcome of the multiphase-field simulations that primary solidification took place as δ whereas the γ-formation was predominantly accomplished in solid-state and promoted among the δ interfaces as their growth was stimulated through the Mn-enriched regions (Fig. 5**a** and **b**).

Secondly, during rapid re-heating, the areas below the melt pools were subjected to temperatures above the onset γ-formation temperature Ae_3. Consequently, γ-reversion/nucleation can take place on lath, packet or block boundaries of the α´ or on prior γ-grain boundaries [51,52]. In the multiphase-field simulations in Fig. 5**a**, nucleation of randomly oriented globular γ-grains was initiated on α´*/ α´* grain

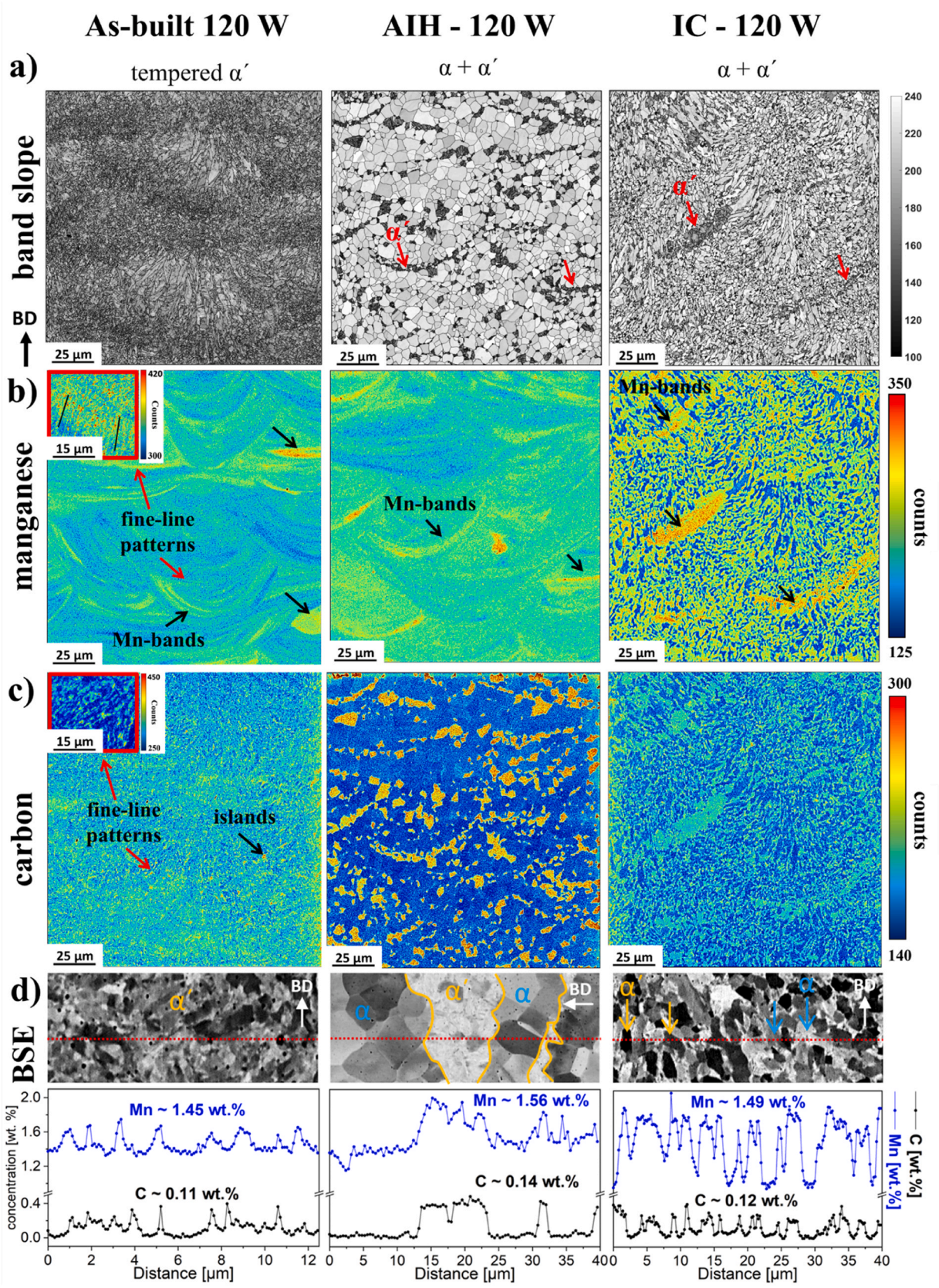

Fig. 6. EPMA results of as-built and heat-treated 120 W samples acquired from the middle of the cross-sections parallel to BD. (a) EBSD band-slope maps. (b) Mn and (c) C intensity maps (in counts). Close-up frames display additional measurements performed to visualize the fine-line Mn and C partitioning in more detail. (d) EPMA line scans and corresponding BSE images showing the local C and Mn distribution in the as-built and heat-treated 120 W samples. The red dashed lines represent the locations of the line-scans. Orange and blue colors show α´ and α, respectively.

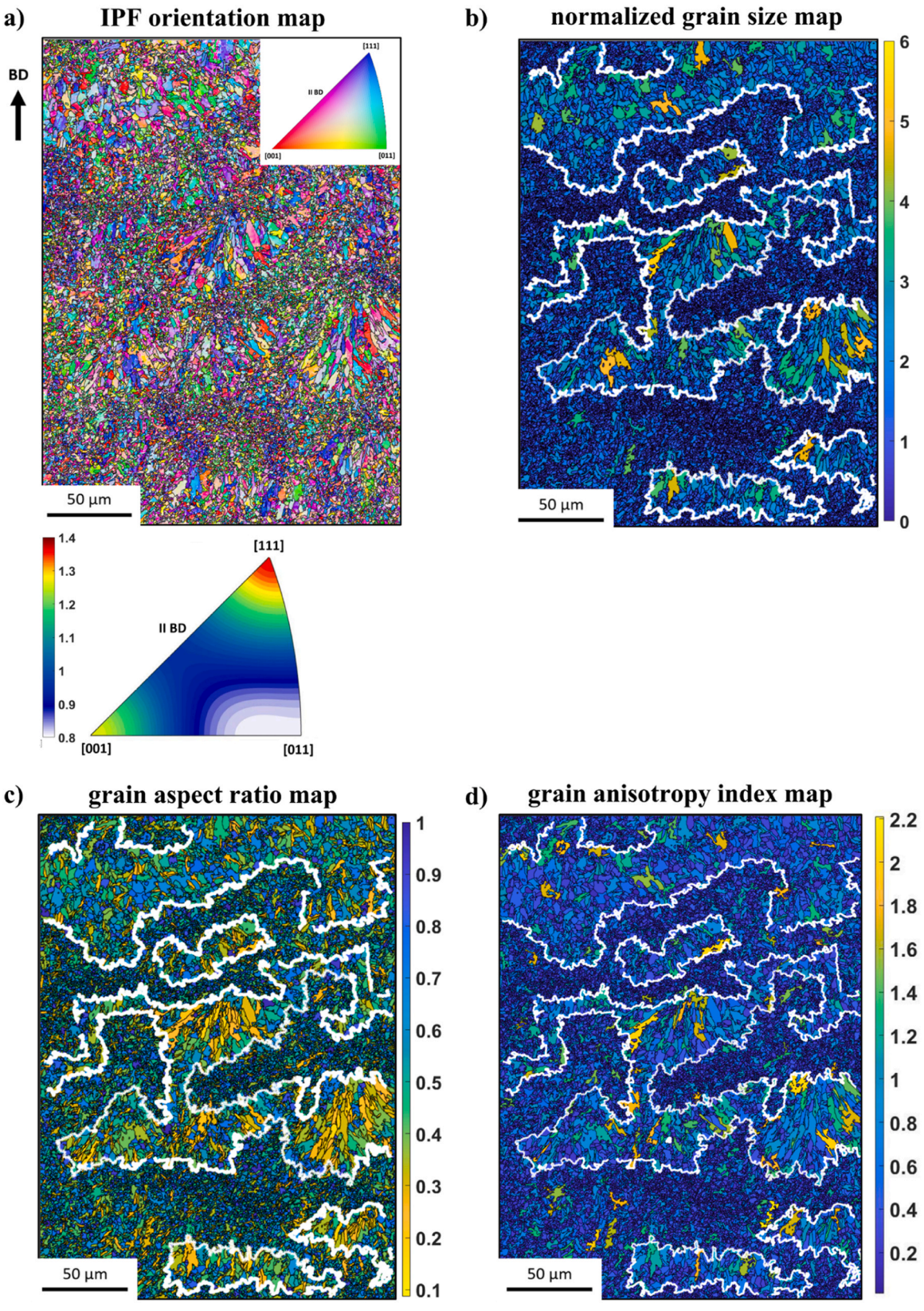

Fig. 7. EBSD analysis of the as-built 120 W state. Representative EBSD images were acquired from the center of the cross-section parallel to BD, and the corresponding color coding is given for each analysis. The white contours display the cluster boundaries of coarse- and fine-grained clusters. (a) EBSD inverse pole figure (IPF) orientation maps and the corresponding IPF showing the crystallographic orientation distribution. (b) Normalized grain size maps, (c) grain aspect ratio maps and (d) grain anisotropy index map.

boundaries (which in the simulation represent the former δ/δ-interfaces that have undergone the transformations δ → γ →α´→ α´* during rapid cooling and reheating). The growth of fresh γ-grains into the parent α´* eventually resulted in refinement of grains in the previously deposited layer. Upon subsequent rapid cooling, fine γ-grains mainly transformed to α´, as morphologically visible in Fig. 3**b.** Ultimately, temporal evolution of the thermal profiles along the melt pool and the consecutive solid-state transformations of δ → γ and γ ↔ α´ resulted in

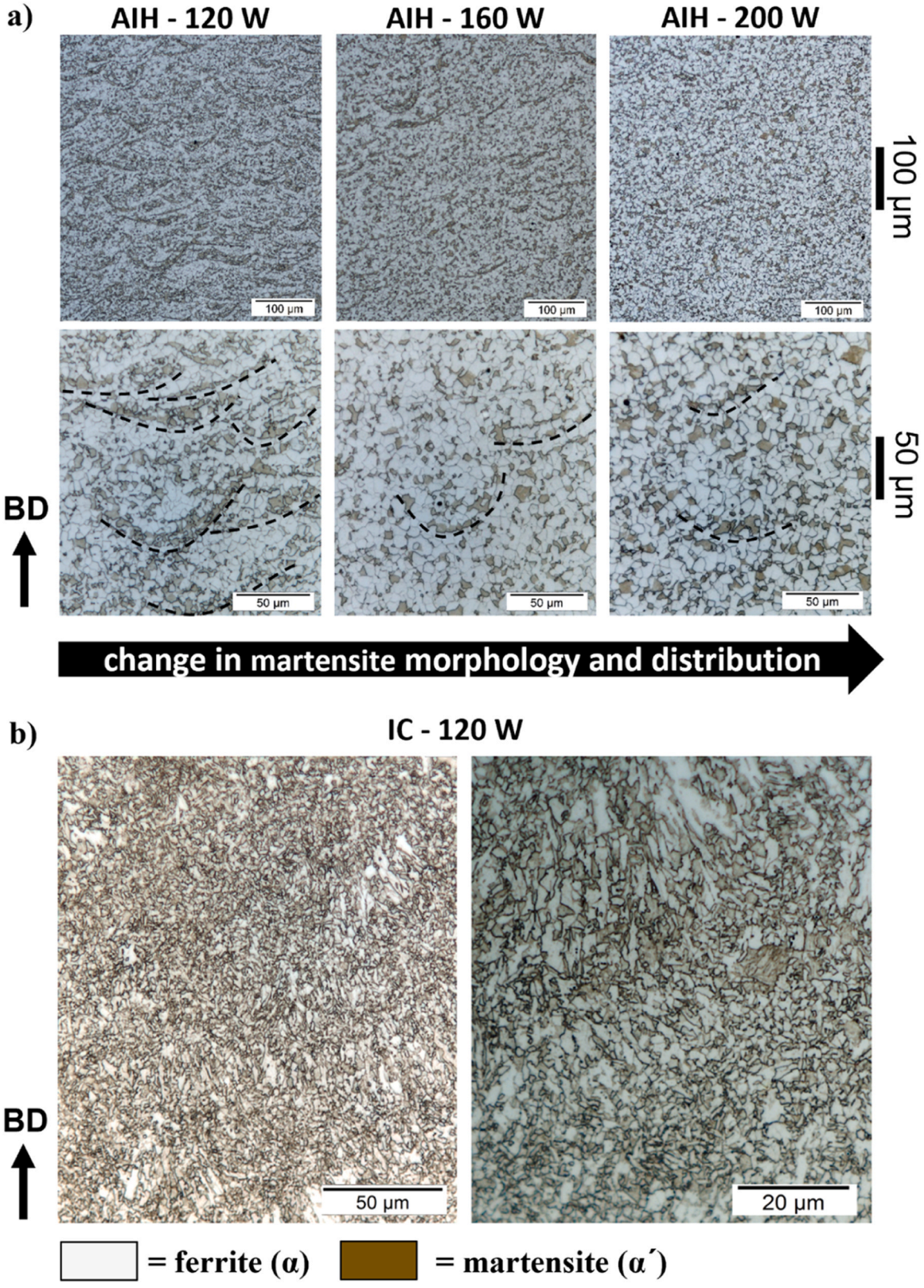

Fig. 8. Optical micrographs of the (a) AIH–treated and (b) IC-treated samples. Black dashed lines in (a) indicate martensite bands located at prior melt pool boundaries.

formation of morphological heterogeneities governed by the spatial grain size differences of PAGs, in combination with the weak (almost random) texture of α′.

3.3. Influence of post-heat treatments on microstructure evolution

The qualitative and quantitative distribution of Mn and C was obtained by EPMA maps and line scans, respectively, for the heat-treated states, as shown in Fig. 6. Optical micrographs of the heat-treated states were displayed in Fig. 8, and the corresponding microstructures were characterized by SE and in-lens micrographs, as shown in Fig. 9. The α′ (area) fractions determined from the optical micrographs are presented in Table 4. The microstructure of the heat-treated 120 W samples were characterized by EBSD in terms of crystallographic orientation and grain morphology distributions and compared with the as-built 120 W state, as represented in Fig. 10.

Regardless of the L-PBF parameters and the heat-treatment strategy, the tempered α′ in the as-built state transformed to ferrite (α) (smooth surface with no substructure) and α′ dual-phase microstructure (Fig. 8 and Fig. 9). EPMA maps and line scans (Fig. 6) revealed that Mn partitioning on prior melt-pool boundaries was preserved for both heat-treated states, whereas spatial distribution of Mn and C was closely related to the phase distribution, since Mn and C were depleted in α and enriched in α′. Similar to the weak (almost random) texture observed in as-built 120 W state, the subsequent AIH and IC heat-treatments resulted in a weak texture with allocation of the <111> and <001>|| BD

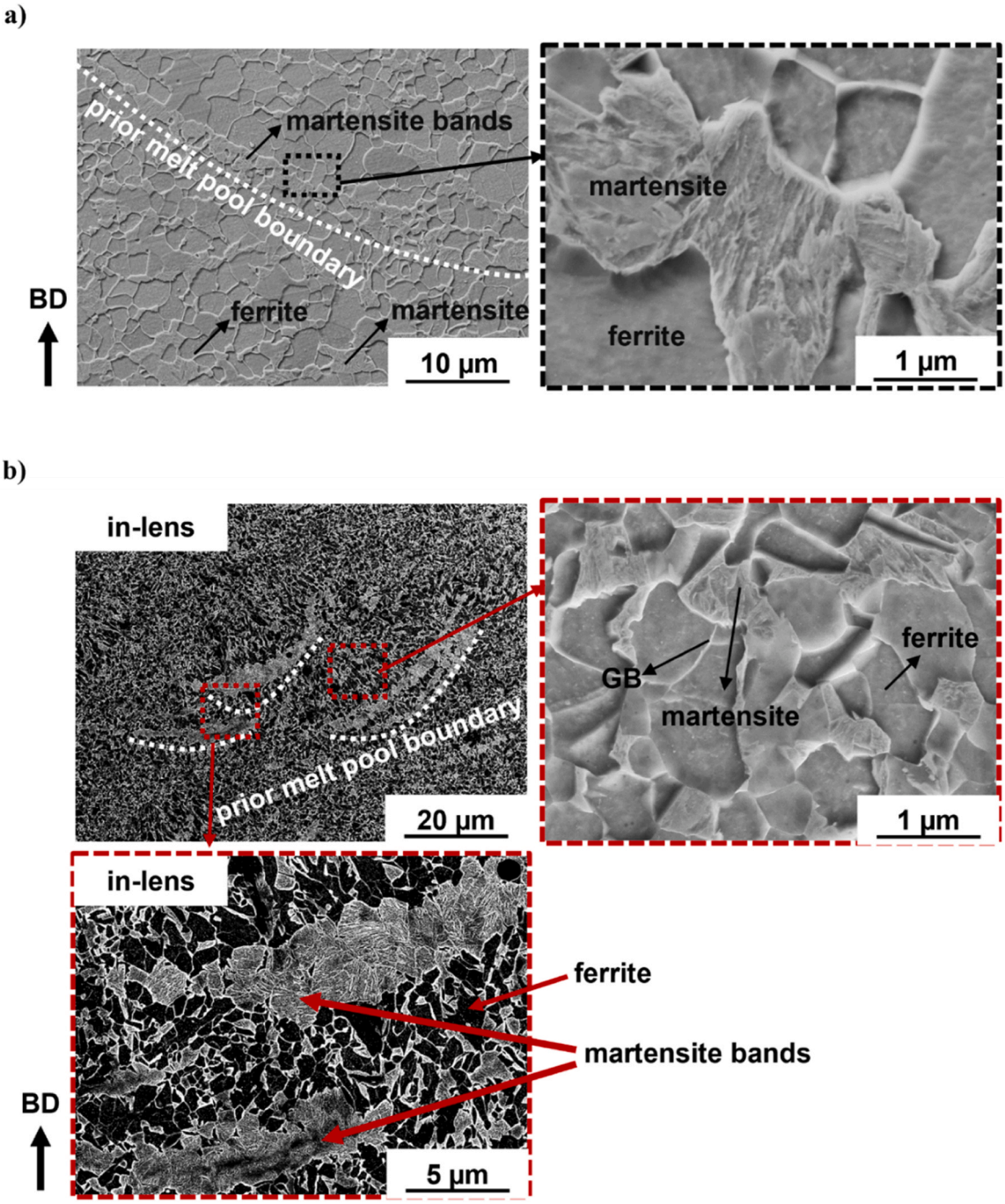

Fig. 9. SE and in-lens micrographs of the heat-treated samples; (a) AIH – 120 W and (b) IC –120 W states. White dotted lines indicate prior melt pool boundaries. Grain boundaries are indicated by GB.

poles, as shown in the IPF orientation maps and IPF plots in Fig. 10**a**.

The two-step AIH treatment led to significant modification of the grain morphology with respect to the as-built state, as shown in Fig. 8**a** and Fig. 9**a**. A substantial reduction in morphological heterogeneities was observed, as evidenced by the homogeneous grain morphology distributions with respect to the grain size and shape (Fig. 10**b** and Fig. 10**c**). The nominal effective grain size and aspect ratio compared to the as-built 120 W state increased to 3.81 μm (+73 %) and 0.62 (+13 %), respectively (**Table S1**), denoting the effect of complete austenitization followed by nucleation and growth of α during inter-critical holding. In addition, the effective grain anisotropy index was reduced to 22 %, which was a strong indicator of transitioning from elongated grain morphology to near-equiaxed grain morphology distribution. Hence, the two-step AIH treatment facilitated the elimination of the L-PBF-induced clusters of coarse- and fine-grains as well as homogenization of grain morphologies.

Although the AIH treatment resulted in homogeneous grain morphology distribution, Fig. 8**a** and Fig. 9**a** reveal a heterogeneous distribution of α′, which was mainly concentrated in the vicinity of the prior melt pool boundaries in band-like structures. Similar structures of ferrite-pearlite or ferrite-martensite bands are commonly observed in many steels due to the segregation of substitutional alloying elements [53,54]. As displayed in the EPMA elemental maps (Fig. 6) of the as-built 120 W state, Mn was enriched at the prior melt pool boundaries. Since the heat-treatment temperatures and holding times used in this study were not sufficiently high to yield complete elemental homogenization [55,56], Mn diffusion was limited and the heterogeneous Mn distribution on the prior melt pool boundaries was preserved after post-L-PBF heat-treatments (Fig. 6**b**). Therefore, a heterogeneous distribution of alloying elements was observed in the as-built state governed the local thermodynamics and phase transformation kinetics during the post-L-PBF heat-treatments [57]. The deviation in local Mn concentration influenced the γ stability and fraction (Fig. 1**b,** Table 3). Consequently, the regions enriched in Mn correspond to a relatively low Ae_1 and Ae_3, thus, to a relatively high γ stability during inter-critical holding. Through the austenitization step of AIH treatment, γ initially formed in the regions enriched in Mn (Fig. 6) simultaneously with C redistribution, followed by complete austenitization of the α′ in the as-built microstructure. The subsequent α nucleation during the inter-critical holding step was also affected by the compositional heterogeneity. The α formation initially started in the Mn-depleted regions [58]. Simultaneously, C distribution was governed by the different C-solubilities in γ and α. The C diffusion took place due to its lower solubility in α and concentrated in the surrounding γ/Mn-enriched regions [59,60], where it enhanced the stability of the existing γ. Upon quenching below M_s, γ transformed to α′ in the respective regions by forming α′-islands in the prior melt pools and α′-bands in the perimeter of the prior melt pools. From Fig. 6**b** and **c**, it was evident that the Mn-enriched areas display higher α′ fractions and more pronounced C partitioning as compared to the regions that were relatively depleted in Mn. On the other hand, EPMA line-scans in Fig. 6**d** showed that Mn distribution in α-grains did not exhibit severe fluctuations.

A clear difference in α′ morphology and distribution was observed upon application of AIH treatment depending on the initial L-PBF processing conditions. As shown in Fig. 8**a,** extended bands of curved α′ (along prior melt pool boundaries) were significantly weakened with increasing laser power and replaced with more homogeneously distributed α′-islands. The results indicated that by changing the L-PBF processing parameters, a strong manipulation of α and α′ distribution can be achieved upon post heat-treatments due to varying evolution of the HAZ (e.g., thermal profiles, chemical distributions, melt pool sizes). In addition, the α′ fractions were found to be around ~30 % for all AIH conditions, as presented in Table 4. This indicates that decarburization and Mn evaporation during the L-PBF process had only a minor effect on the overall α′ fraction after the AIH treatment.

The as-built 120 W samples were heat-treated using single step IC strategy to investigate the microstructure evolution under the absence of an intermediate austenitization step. The microstructure of the IC - 120 W state showed a strong similarity to the grain morphology distribution of the as-built 120 W sample, i.e., conservation of the columnar grain morphology, fine- and coarse-grained clusters, as shown in Fig. 10. Moreover, the quantitative relationship between coarse- and fine-grained clusters was also preserved. Despite the increase in effective nominal grain size to 2.7 μm by +22.7 % compared to the as-built 120 W state, the difference between effective grain sizes of coarse- and fine-grained clusters were found to be 1.1 μm in the IC - 120 W state, i.e. similar to that of the as-built state (~1.2 μm) (**Table S1**). In as-built state, the difference in effective aspect ratio of the coarse-grained clusters was 8.9 % lower than that of the fine-grained clusters, whereas the effective grain shape anisotropy index was 45.5 % higher. Similarly, coarse-grained clusters in the IC state exhibited lower effective aspect ratio by 5.4 % and higher effective grain shape anisotropy index by 41.9 %, as compared to those of the fine-grained clusters. The morphology analysis indicated the preservation of the characteristic as-built microstructure consisting of distinct coarse- and fine-grained clusters with low aspect ratios (i.e., elongated grain shapes) and the associated morphological heterogeneities despite the grain growth during the IC treatment.

Another aspect of morphological heterogeneities corresponds to the grain major axis (grain shape-axis) orientation (ω),[1] which was defined as the angle between the major axis of the best-fit ellipse to the grain section and a reference axis, which was selected as BD (0°). Fig. 11 demonstrates the distribution of grain major axis orientation relative to BD. As shown in Fig. 11, there is a distinct difference between the coarse- and fine-grained clusters with respect to the distribution of grain major axis orientation descriptor ω. The ratio r associated with the coarse-grained clusters of the as-built and IC states was 1.8 and 1.2, respectively, suggesting that the majority of the grains in coarse-grained clusters were oriented almost parallel to BD (i.e., columnar grains). The ratio r corresponding to the fine-grained clusters of the as-built and IC states was 0.8 and 0.6, respectively, implying a high fraction of grains in the fine-grained clusters whose major axis orientation was almost perpendicular to BD. The strong contrast observed in the grain major axis orientation distribution in different cluster types was another indicator that the heterogeneous grain morphology of the as-built state was mostly conserved during the IC treatment.

In Fig. 12, geometrically necessary dislocation (GND) density maps in correlation with STEM micrographs, were shown. It is visible that the mean density of GNDs in as-built 120 W state reduced from 1.4×10^{15} to 7.8×10^{14} m^{-2} (Fig. 12**a**) in IC – 120 W state. For IC - 120 W state, higher GND densities were observed for fresh α′-islands that were

Table 4
Martensite (α′) area fractions determined for the heat-treated states given in Fig. 8. Area fractions were calculated from at least 3 different micrographs with post-image processing.

Heat-treatment - Laser Input	**α′** area fraction [%]
AIH – 120 W	32.7 ± 0.4
AIH – 160 W	27.7 ± 1.2
AIH – 200 W	32.2 ± 1.0
IC – 120 W	44.9 ± 1.5

[1] ω is a continuous variable ranging from 0° to 90° ($0° \leq \omega \leq 90$). $\omega = 45°$ was selected as a threshold to assess the grain shape-axis orientation. $\omega < 45°$ indicates that the grain major axis has a relatively low angle with respect to BD, while $\omega > 45°$ indicates that the grain major axis has a relatively high angle with respect to BD. Therefore, another morphological descriptor associated with grain shape-axis orientation was defined, which is the ratio of the (area) fraction of grains whose major axis has a relatively low angle with BD ($f(\omega < 45°)$) to the fraction of grains whose major axis has a relatively high angle relative to BD ($f(\omega > 45°)$): $r \equiv \frac{f(\omega<45°)}{f(\omega>45°)}$.

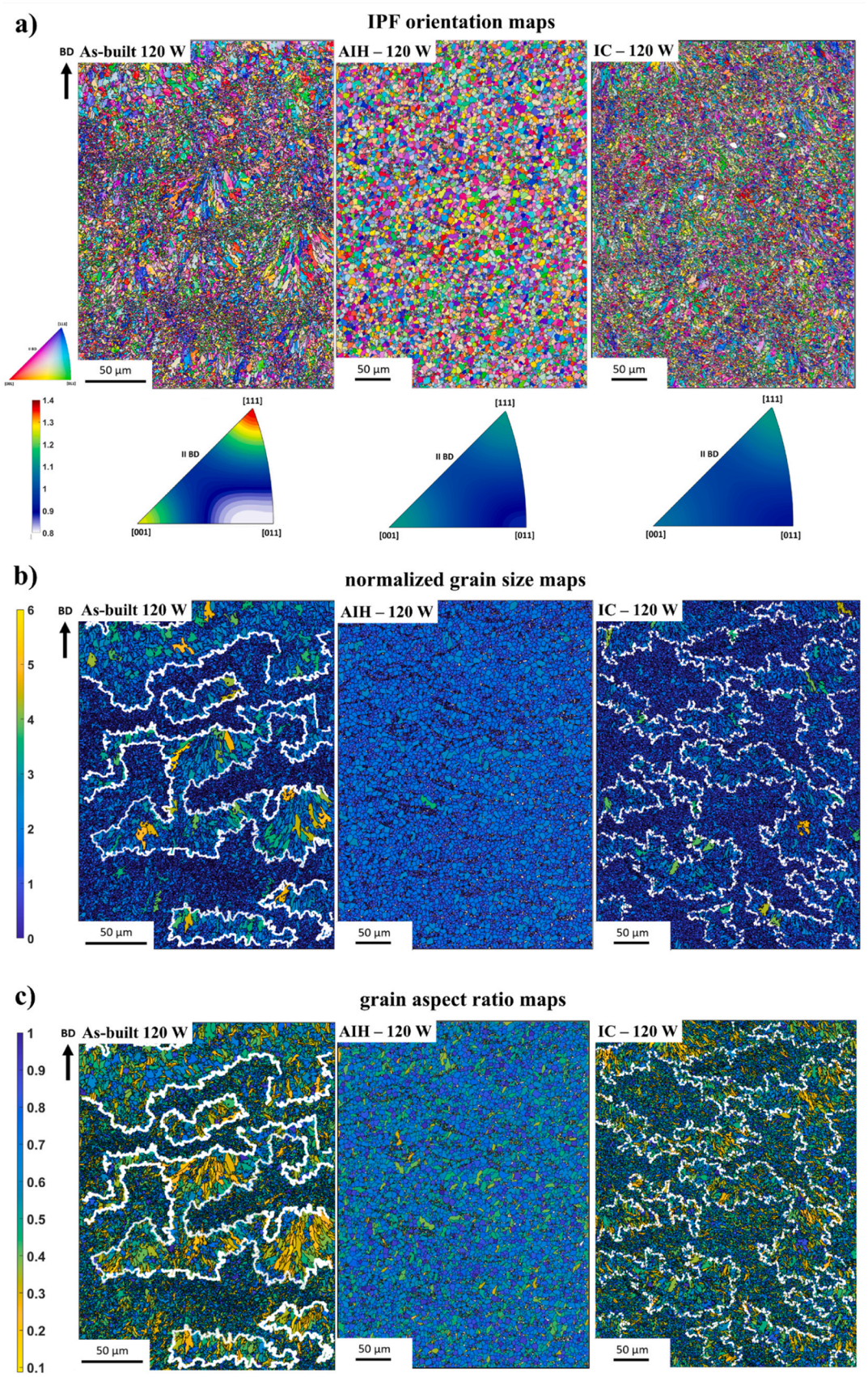

Fig. 10. EBSD analysis of the as-built and heat-treated 120 W samples. Representative EBSD images were acquired from the middle of the cubic cross-section parallel to BD. White contours display the cluster boundaries of coarse- and fine-grained clusters. (a) EBSD inverse pole figure (IPF) orientation maps and corresponding IPFs, (b) normalized grain size maps and (c) grain aspect ratio maps.

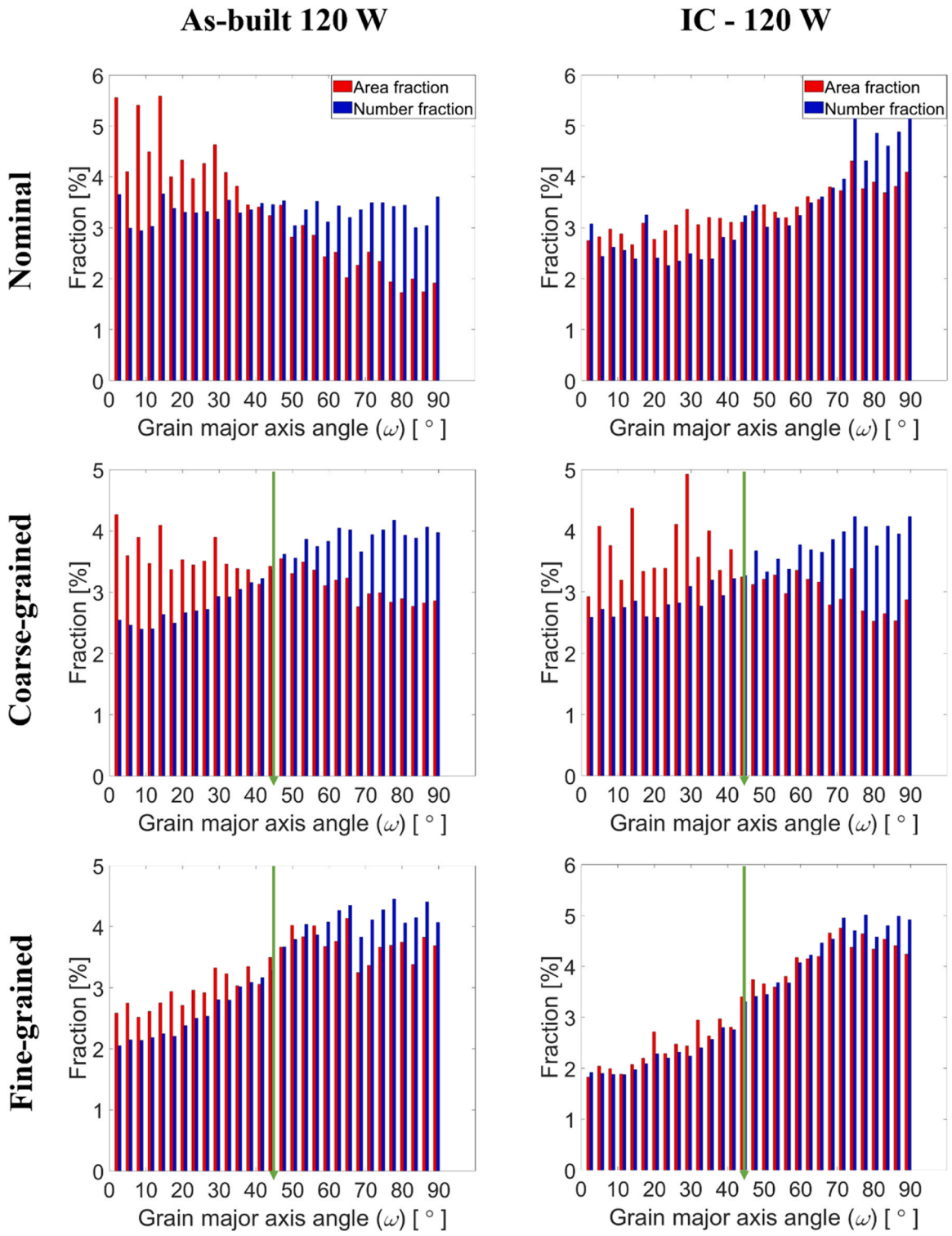

Fig. 11. Histograms of the distributions of the grain major axis angle (grain shape-axis orientation) ω in given states with respect to the building direction (0°). Green lines indicate $\omega = 45°$ as the threshold between columnar (ω <45°) and horizontal (ω >45°) grains.

mainly concentrated on grain and prior melt pool boundaries, whereas α-grains exhibited lower GND densities. Correlative GND density maps and STEM images (Fig. 12**b**) revealed that the dislocations in as-built martensitic microstructure were partly annihilated/recovered in α-grains obtained after IC heat-treatment. In addition, fresh α′-islands with higher dislocation densities were formed on the boundaries of the α-grains.

During the single-step IC treatment, complete austenitization was absent and the α′ fraction increased to 44.9 ± 1.5 % (Table 4), as a result of the elevated inter-critical annealing temperature and holding time leading to an increase in equilibrium γ content [57] (Fig. 1**b,** and Table 3). The curved α′-bands in the vicinity of the prior melt pool boundaries are visible in analogy to the AIH – 120 W state (Fig. 9**b**). In contrast to the AIH – 120 W state, α′ formation was not restricted to the Mn-enriched bands in the vicinity of the prior melt pool boundaries. As shown in Fig. 9**b**, α′ also formed as finely dispersed islands distant from

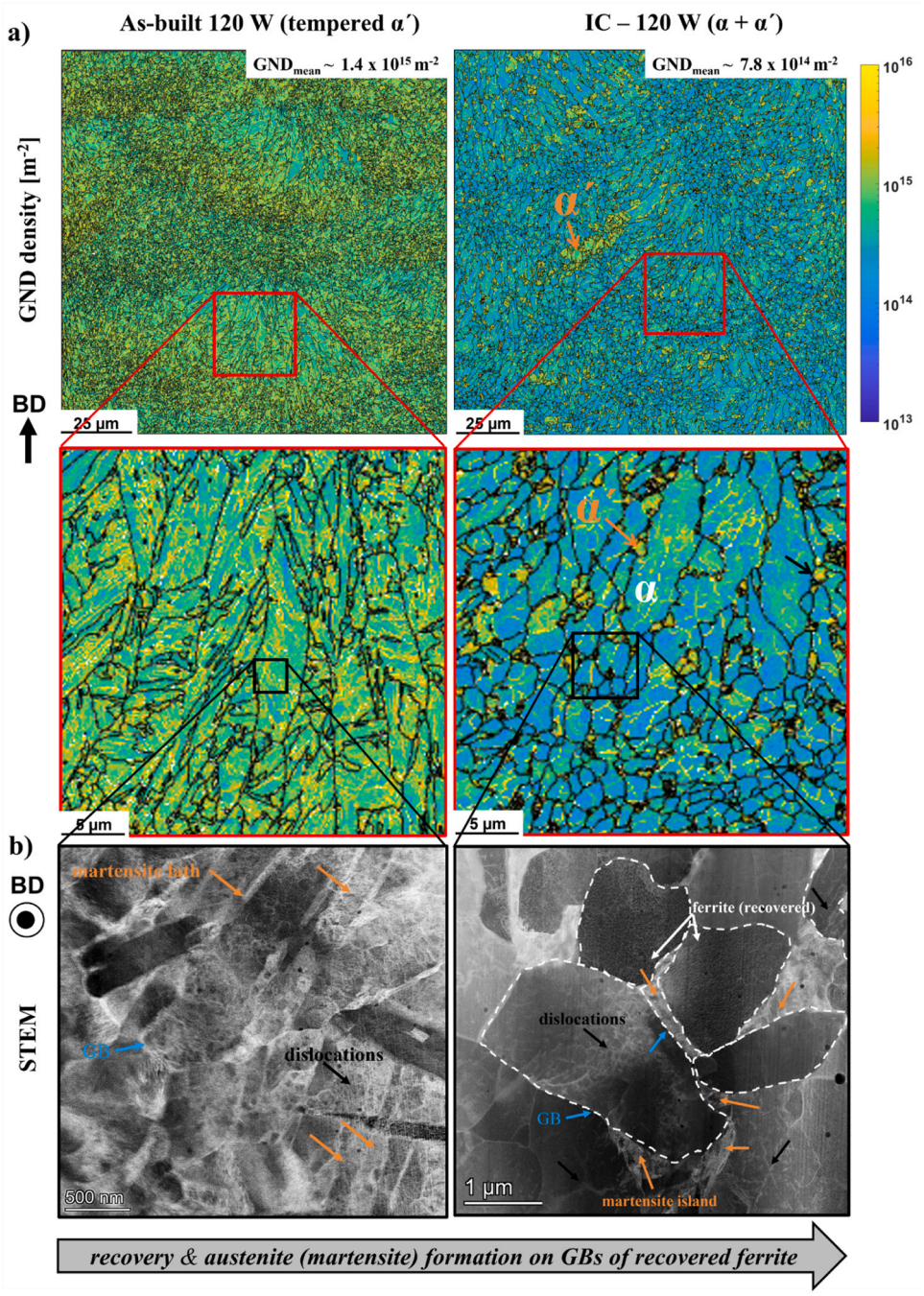

Fig. 12. Evolution of microstructural features upon IC-treatment. (a) EBSD geometrically necessary dislocation (GND) density maps taken from the same area as the EPMA measurement shown in Fig. 6. (b) STEM-LAADF micrographs of ferrite grains, fine martensite islands, dislocation substructures, and grain boundaries represented by white, orange, black and blue arrows, respectively. The lamellae were extracted parallel to BD.

the prior melt pool boundaries (e.g., regions associated with the columnar grains). The morphological heterogeneities in as-built 120 W state were preserved in the IC – 120 W state that resulted in the distribution of α and α′ dual-phase microstructure in characteristic as-built grain morphology distribution (see Fig. 10 and Fig. 11). This phenomenon was mainly related to the influence of microstructural heterogeneities in different length-scales that were effectively utilized by the selected IC heat-treatment strategy. This indicates that the Mn partitioning was to a large extend inherited from the as-built state (Fig. 6**d**), which itself resulted from the Mn-partitioning during the δ-ferrite solidification (Fig. 5**b**). During subsequent inter-critical annealing at 800 °C, the as-built α′ microstructure (distorted bcc) was heat treated in the α (bcc) and γ (fcc) phase-field (Fig. 1**b**). Hence, there was essentially a negligible driving force for nucleation of fresh α-grains in contrast to the fresh γ-grains, as also supported by the columnar (preserved) shape of the α-grains (Figs. 10 and 11). Therefore, α was rather expected to form via C-diffusion out of the C-rich α′, as it tends to reach its equilibrium composition, whereas γ nucleation occurred through the C diffusion towards Mn-enriched interfaces. From the EPMA maps and line scans in Fig. 6 it is clearly visible that the C and Mn distribution coincides with the grains associated with α′, whereas Mn and C were depleted in α-grains. This indicates Mn and C partitioning in γ during the inter-critical annealing. Moreover, elongated α′ (tempered) grains in as-built 120 W state exhibited higher dislocation densities (Fig. 12**a** and

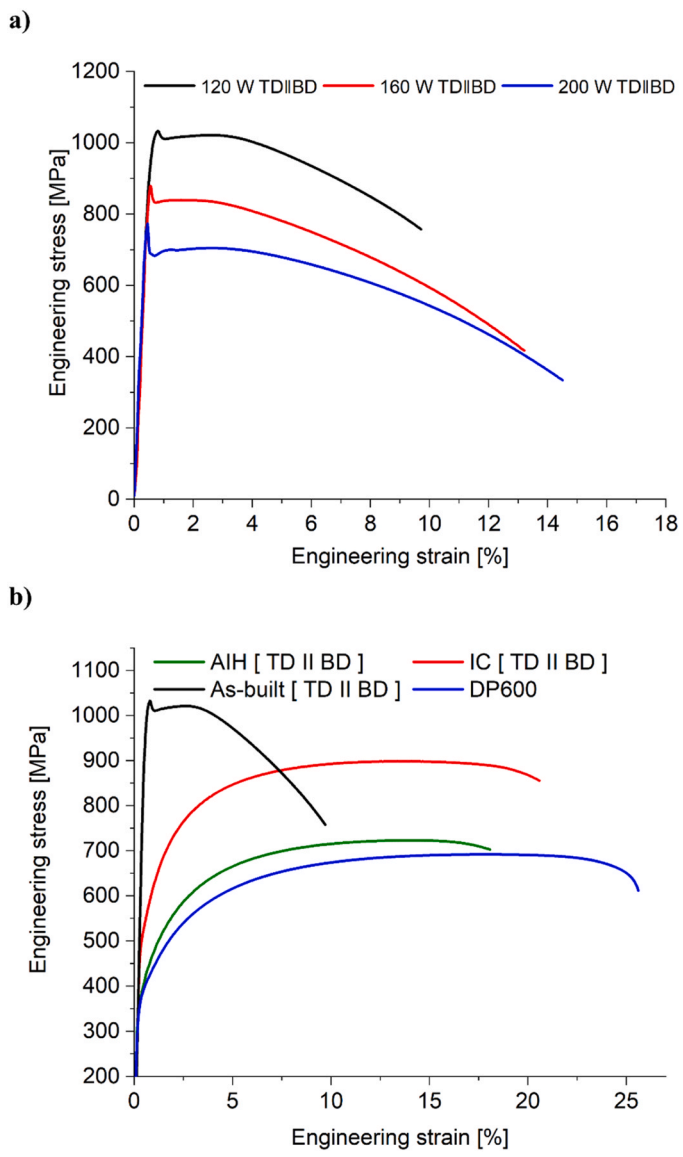

Fig. 13. Engineering stress-strain curves of (a) the as-built and (b) heat-treated states. The tensile direction (TD) was parallel to BD (TD || BD). A thermo-mechanically processed DP600 steel was used for comparison in (b).

b) as compared to the IC – 120 W state (Fig. 12**a**) due to the static recovery during IC heat-treatment (quantitatively and visually seen by close-up GND maps and STEM images in Fig. 12, respectively). Furthermore, α′-grains at grain boundaries were characterized by higher GND densities than the α-grains, indicating that fresh α′ was formed on α-interfaces. Consequently, γ formation was expected to be initiated by nucleation at α′-grain and -lath boundaries due to annihilation of dislocations from parent α′ (Fig. 12) and strong interface segregation of the γ stabilizing elements (Fig. 6**b**, **c** and **d**) [61,62]. As a result of this mechanism, α exhibits an elongated post-martensitic morphology (Fig. 10 and **Table S1**), as it originated from recovered α′ with decreased C content (Fig. 6**b** and **d**). The freshly formed α′ was finely dispersed along the α-grain boundaries (Fig. 12) where the Mn and C partitioning was observed (Fig. 6**b**, **c** and **d**). Therefore, the IC treatment did not result in morphology homogenization as observed for AIH – 120 W state. Evidently, the absence of austenitization treatment effectively aided the distribution of ferritic-martensitic dual-phase microstructure in characteristic L-PBF grain morphology distribution.

3.4. Tensile properties

The engineering stress-strain response of the as-built and heat-treated states are shown in Fig. 13 and the characteristic tensile properties are summarized and compared with a thermo-mechanically processed DP600 steel in Fig. 14. The as-built states exhibited high yield strengths ranging from 0.77 to 1 GPa (Fig. 13**a**). Regardless of the L-PBF process parameters, each as-built state showed a negligible strain-hardening capacity and yield point phenomena.

The occurrence of a discontinuous yield point was related to segregation of carbon atoms to dislocations [42,63], which is a commonly observed phenomena in low-carbon low-alloy bcc steels. Such an effect leads to drastic pinning of dislocations which diminishes the number of free dislocations. Once the yield point has been reached for discontinuous transition, plastic deformation is only possible by increasing the force, which normally leads to strain hardening, necking and subsequent failure. However, in current study, all as-built states showed negligible strain hardening. The absence of notable strain hardening of the as-built states was associated with the high (near saturation) dislocation density in as-built states, at which the rate of generation of mobile dislocations was close to that of annihilation of dislocations. The negligible strain-hardening capacity was also a strong indicator that significant amounts of ductile phases (retained-γ and α) were absent in the as-built states. An increase in laser power from 120 to 200 W resulted in gradual increase in tensile ductility and decreased average yield strength. The higher yield strength of the as-built 120 W sample compared to 160 and 200 W samples was attributed to the variation in L-PBF processing parameters (Table 2) and their corresponding influence on the evolution of the microstructure at various length scales. High temperature gradients and cooling rates resulted in higher (initial) dislocation densities and lower grain sizes, which in turn resulted in high yield strengths [30]. In the present study, the L-PBF process with 120 W laser energy input rendered the highest cooling rates and steepest temperature gradients. This resulted in the generation of a relatively high initial dislocation density (1.4×10^{15} m^{-2}), finer laths and packets of the martensitic microstructure (effective grain size 2.2 μm), which was controlled by the prior austenite grain size (**Figure S6 and S7**). Eventually, high-initial dislocation density and smaller grain sizes (grain boundary strengthening) in as-built 120 W state revealed the strongest contribution to the yield strength. In contrast, samples processed with 160 and 200 W showed lower initial dislocation densities (0.43×10^{15} m^{-2} for 200 W, **Fig. S10**) and larger grains (effective grain size is 3.0 μm for 200 W) due to the above explained phenomenon. Consequently, samples showed lower yield strength whereas the strain accommodation (ductility) was improved owing to the comparatively lower initial dislocation densities than as-built 120 W state.

The tensile properties of the as-built 120 W state were significantly influenced by subsequent heat-treatments. The ferritic-martensitic dual-phase microstructure obtained by AIH and IC strategies resulted in an appreciable drop in yield strength and a significant increase in ductility as well as strain hardening capacity. As shown in Fig. 14, ferritic-martensitic dual-phase steels generally do not show a distinct yield point, but experience rather smooth transition from elastic to plastic deformation [64]. Owing to the composite soft-matrix/hard-reinforcement microstructure of ferritic-martensitic DP steels, the plastic deformation is initially activated in the soft α-matrix, where the high localized initial residual stress (attributed to quenching after post-heat treatments) and high density of mobile dislocations triggers the plastic flow in α at low plastic strains. As a consequence, yielding takes place earlier and at multiple locations in α which suppresses the discontinuous yielding and leads to high early-stage strain hardening [13,64]. The tensile test results imply that the yield and tensile strengths of AIH - 120 W state are comparable with the thermo-mechanically processed DP600 steel, while the AIH - 120 W show lower tensile elongation by approximately 7 %.

The IC – 120 W state exhibited an appreciable increase in yield and tensile strength accompanied by an improvement of the total tensile

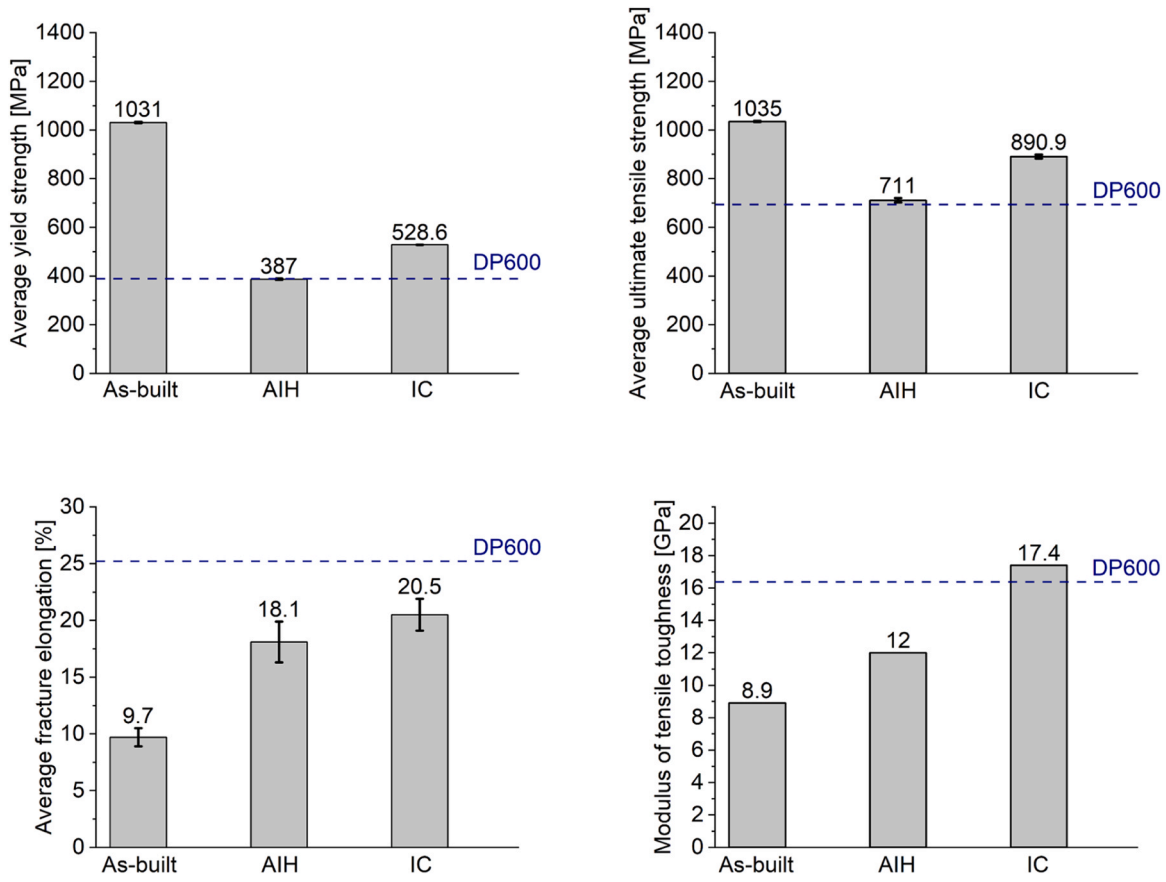

Fig. 14. Comparison of average yield strength, ultimate tensile strength, tensile elongation and modulus of tensile toughness for as-built and heat-treated states of 120 W samples (TD || BD). Error bars demonstrate the standard deviation. Dashed lines show the mechanical properties of reference DP600 steel.

elongation. The increase in yield strength was mainly attributed to the increase in α′ volume fraction [65,66] and also to smaller effective grain sizes compared to the AIH state. Furthermore, the modulus of tensile toughness[2] of the investigated states and the reference DP600 were compared as shown in Fig. 14. Compared to the as-built 120 W state, the heat treatments increased the modulus of tensile toughness drastically, indicating a significant improvement of the energy absorption capacity. The modulus of tensile toughness of the IC – 120 W samples increased almost twice compared to those of the as-built 120 W samples.

Interestingly, the high α′ content and preservation of morphological heterogeneities has not impaired the tensile ductility of the IC – 120 W state. Tasan et. al. [67] showed that the strain localization and failure is influenced by the characteristics of the dual-phase microstructures, e.g., α and α′ grain size, their distribution and fractions. Hence, the tensile properties of the IC – 120 W state improved in two-ways, e.g., based on the heterogeneous α-grain size in coarse- and fine-grained clusters accompanied by relatively fine α′-islands along the α-interfaces. Firstly, the fine-grained clusters with finer α-grains contributed to the high yield strength and enhanced strain hardening, while the coarse-grained clusters with relatively coarser α-grains contributed to accommodation of plastic strain and energy dissipation. Similar contributions on combination of high strength and ductility were reported in other additively manufactured metals with heterogeneous, clustered microstructures [68,69]. Secondly, the relatively small and homogeneously dispersed α′-islands allows more ferritic regions to contribute to the accommodation of the plastic deformation through fine strain bands created throughout the ferritic matrix [67]. Hence, by distribution of the ferritic-martensitic dual-phase microstructure in L-PBF specific grain morphology, earlier strain localization was prevented, and superior tensile properties were obtained.

4. Conclusions

In the present study, a low-alloy steel was processed via the metal additive manufacturing technique laser-powder bed fusion (L-PBF). A combination of experimental and computational methods was used to facilitate a better fundamental understanding of the liquid-solid and solid-solid phase transformation mechanisms and resulting microstructure evolution of low-alloy steels during L-PBF. The evolution of compositional and morphological heterogeneities during L-PBF and subsequent post-L-PBF heat treatments as well as their influence on the plastic deformation behavior was discussed. The following conclusions can be drawn:

I. L-PBF of low-alloy steel revealed compositional and morphological heterogeneities in as-built state. Compositional heterogeneities are correlated with Mn and C partitioning along the melt pools, whereas the morphological heterogeneities are associated with the emergence of distinct coarse- and fine-grained clusters. Multiphase-field simulations and microstructure characterization unveiled that consecutive phase transformations of liquid → delta-ferrite (δ), δ → austenite (γ), and γ ↔ martensite (α′) governed the C distribution, whereas Mn the distribution was solely controlled by δ solidification. Moreover, the multiphase-field simulation uncovered that cluster formation was primarily induced by solid-state phase transformations, with δ → γ leading to the formation of coarse-

[2] Modulus of tensile toughness is the maximum amount of energy per unit volume ($\frac{J}{m^3} \equiv$ Pa) absorbed before fracture under uniaxial tension, which is the area underneath the engineering stress-strain curves plotted in Fig. 13**b**.

grains and γ ↔ α′ contributing to grain refinement and the development of fine-grains in the heat affected zone (HAZ).

II. The as-built state exhibited a martensitic (tempered) microstructure with a weak (almost random) texture. The martensitic microstructure and texture weakening emerged due to the consecutive solid-state phase transformations initially by means of δ → γ and later by γ ↔ α′ throughout the L-PBF process.

III. The post-L-PBF heat-treatments invoked the formation of ferritic-martensitic dual-phase (DP) microstructures with heterogeneous α′ distribution due to α′-banding in the perimeter of the prior melt pool boundaries. The formation of α′-bands is correlated to locally lower Ae_1 and Ae_3 temperatures controlled by Mn enrichment, leading to relatively high γ stability in the vicinity of the prior melt pool boundaries during inter-critical holding.

IV. The austenitization step during AIH heat treatment resulted in a homogeneous morphology distribution, whereas direct inter-critical annealing (IC, without austenitization) facilitated retainment of the morphological heterogeneities formed during L-PBF. In the latter case, ferrite (α) formed due to recovery of and C-diffusion from α′, thus maintaining the elongated grain morphology of the α′ obtained after L-PBF. Thus, IC heat-treatment resulted in the distribution of α and α′ DP microstructure within the unique grain morphology distribution (coarse- and fine-grained clusters) established after L-PBF.

V. IC heat-treatment enabled high yield (528.6 MPa) and ultimate tensile (890 MPa) strength due to the conservation of the L-PBF-specific microstructural heterogeneities. As such, distribution of α and α′ in characteristic fine- and coarse-grained clusters promoted enhanced accommodation of plastic strain ($\varepsilon_{fracture} = 20.5$ %).

CRediT authorship contribution statement

Ahmet Turnali: Visualization, Software, Methodology, Investigation, Formal analysis, Conceptualization, Writing - original draft, Writing - review & editing. **S. Amir H. Motaman:** Methodology, Formal analysis, Investigation, Software, Writing - review & editing. **Yuling Chang:** Investigation, Conceptualization, Methodology, Writing - review & editing. **Bernd Böttger:** Software, Methodology, Formal analysis, Writing - review & editing. **Alexandros Serafeim:** Conceptualization. **Lennart Sayk:** Investigation. **Nicolas J. Peter:** Investigation. **Silvia Richter:** Investigation. **Alexander Schwedt:** Investigation. **Simon Höges:** Resources. **Christian Haase:** Supervision, Funding acquisition, Conceptualization, Methodology, Writing - review & editing.

Declaration of Competing Interest

The authors declare that they have no known competing financial interests or personal relationships that could have appeared to influence the work reported in this paper.

Data availability

Data will be made available on request.

Acknowledgements

This study has been funded by the German Federal Ministry of Education and Research (BMBF) under the NanoMatFutur project “MatAM - Design of additively manufactured high-performance alloys for automotive applications” (Project ID: 03XP0264). This work contains results obtained from experiments performed at the Ernst Ruska-Centre (ER-C) for Microscopy and Spectroscopy with Electrons at the Forschungszentrum Jülich (FZJ) in Germany [https://doi.org/10.17815/jlsrf-2–106, https://doi.org/10.17815/jlsrf-2–68]. The ER-C beamtime access was provided via the DFG Core Facility Project (FZJ_IEK-2_PN1).

Appendix A

Description of the phase-field model

MICRESS® employs the phase-field method, in which interfaces are not explicitly tracked as in classical sharp interface models. Instead, the phase-field method represents interfaces through an order parameter that is integrated into the solution. In this method, the evolution of a multi-phase microstructure is depicted using a set of multi-phase-field variables $\phi_{\alpha=1.\nu}(x,t)$ in both space and time. The phase-field parameter takes the value of $\phi_\alpha = 1$ within the phase or grain region and $\phi_\alpha = 0$ in the area surrounding the phase or grain. At the interface, the parameter ϕ_α undergoes a continuous variation between 0 and 1 across the interfacial thickness (η). It’s important to note that ϕ_α should be regarded as a local phase-field variable subject to a unity sum constraint.

$$\sum_{\alpha=1}^{\nu} \phi_\alpha(\vec{x},t) = 1 \tag{1}$$

The free energy function F, which comprises contributions from the interface free energy density f^{intf}, and the thermodynamic free energy density, f^{th}, governs the time evolution of ϕ_α by integrating the density functional contributions across the domain Ω.

$$F(\{\phi_\alpha\},\vec{c}\,) = \int \left[f^{th}(\{\phi_\alpha\},\vec{c}\,) + f^{intf}(\{\phi_\alpha\})\right] d\Omega \tag{2}$$

In Eq. (2), f^{th} can be established by taking into account that each unit of the volume element is a mixture of phases, with a fraction ϕ_α and concentration $\vec{c}_\alpha$, which comprises the solute portioning through the Lagrange term. On the other hand, f^{intf} can be extended with $\phi_\alpha = 1.\nu$, encompassing the interfacial energy $\sigma_{\alpha\beta}$ between the local phases ν.

$$f^{th}(\{\phi_\alpha\},\vec{c}\,) = \sum_{\alpha=1}^{\nu} \phi_\alpha f_\alpha(\vec{c}_\alpha) + \sum_{i=1}^{n-1}\left(c^i - \sum_{\alpha=1}^{\nu}\phi_\alpha c_\alpha^i\right)\tilde{\mu}^i \tag{3}$$

$$f^{intf}(\{\phi_\alpha\}) = \sum_{\alpha=1}^{\nu}\sum_{\beta=\alpha+1}^{\nu}\frac{4\sigma_{\alpha\beta}}{\eta}\left[\phi_\alpha\phi_\beta - \frac{\eta^2}{\pi^2}\nabla\phi_\alpha\nabla\phi_\beta\right] \tag{4}$$

Throughout the phase transformation process, the temporal evolution of the phase-field parameter is guided by the minimization of the free energy based on the relaxation principle. This relaxation method remains agnostic to the particular combinations of phases involved, while the kinetics of the

evolution is governed by the mobility $M^{\phi}_{\alpha\beta}$, which is defined uniquely for each combination of phases.

$$\dot{\phi}_\alpha = \sum_{\beta\neq\alpha}^{\nu} M^{\phi}_{\alpha\beta}\left[\left(\frac{\delta F(\{\phi_\alpha, \vec{c}\})}{\delta\phi_\beta}\right)_{\phi_\gamma\neq\beta} - \left(\frac{\delta F(\{\phi_\alpha, \vec{c}\})}{\delta\phi_\alpha}\right)_{\phi_\gamma\neq\alpha}\right] \tag{5}$$

Ultimately, the phase-field equation is formulated by incorporating anisotropic properties into the free energy density functional and the phase-field relaxation approach, resulting in the expression:

$$\dot{\phi}_\alpha = \sum_{\beta\neq\alpha}^{\nu} \widetilde{M}^{\phi\alpha}_{\alpha\beta}\left[b\Delta G_{\alpha\beta} - \sigma^{\sigma}_{\sigma\beta}K^{\alpha}_{\alpha\beta} + \sum_{\gamma\neq\beta\neq\alpha}^{\nu} J^{\alpha}_{\alpha\beta\gamma}\right] \tag{6}$$

$$K^{\alpha}_{\alpha\beta} = \frac{\pi^2}{2\eta^2}(\phi_\beta - \phi_\alpha) + \frac{1}{2}(\nabla^2\phi_\beta - \nabla^2\phi_\alpha) + \frac{1}{a^{\sigma}_{\alpha\beta}}\sum_{i=1}^{3}\nabla_i\left[\left(\frac{\partial a^{\sigma}_{\alpha\beta}}{\partial\nabla_i\phi_\beta} - \frac{\partial a^{\sigma}_{\alpha\beta}}{\partial\nabla_i\phi_\alpha}\right)\left(\frac{\pi^2}{2\eta^2}\phi_\alpha\phi_\beta - \frac{1}{2}\nabla\phi_\alpha\nabla\phi_\beta\right)\right] - \frac{1}{a^{\sigma}_{\alpha\beta}}\nabla a^{\sigma}_{\alpha\beta}(\nabla\phi_\beta - \nabla\phi_\alpha) \tag{7}$$

$$J^{\alpha}_{\alpha\beta\gamma} = \frac{1}{2}\left(\sigma^{o}_{\beta\gamma}a^{\sigma}_{\beta\gamma} - \sigma^{o}_{\alpha\gamma}a^{\sigma}_{\alpha\gamma}\right)\left(\frac{\pi^2}{\eta^2}\phi_\gamma + \nabla^2\phi_\gamma\right) + \sigma^{o}_{\alpha\gamma}\sum_{i=1}^{3}\nabla_i\left[\left(\frac{\partial a^{\sigma}_{\alpha\gamma}}{\partial\nabla_x\phi_\alpha}\right)\left(\frac{\pi^2}{2\eta^2}\phi_\alpha\phi_\gamma - \frac{1}{2}\nabla\phi_\alpha\nabla\phi_\gamma\right)\right] - \sigma^{o}_{\beta\gamma}$$
$$\times\sum_{i=1}^{3}\nabla_i\left[\left(\frac{\partial a^{\sigma}_{\beta\gamma}}{\partial\nabla_i\phi_\beta}\right)\left(\frac{\pi^2}{2\eta^2}\phi_\beta\phi_\gamma - \frac{1}{2}\nabla\phi_\beta\nabla\phi_\gamma\right)\right] + \frac{1}{2}\left(\sigma^{o}_{\beta\gamma}\nabla a^{o}_{\beta\gamma} - \sigma^{o}_{\alpha\gamma}\nabla a^{o}_{\alpha\gamma}\right)\nabla\phi_\gamma \tag{8}$$

In this context, the rescaled phase mobility is denoted by $\widetilde{M}^{\phi\alpha}_{\alpha\beta}$, the scaling factor is represented as b, the thermodynamic driving force is $\Delta G_{\alpha\beta}$, the pairwise curvature contribution is $K^{\alpha}_{\alpha\beta}$, and the third-order junction force is introduced $J^{\alpha}_{\alpha\beta\gamma}$ as in Eq. 6. Additionally, an anisotropic function, as described in Eqs. 7 and 8, is designated as $a^{\sigma}_{\alpha\beta}$. The diffusion is computed from the free energy functional using a concentration relation approach within the framework of the mixture approach. This entails replacing the mobilities with those specific to diffusion while adhering to the constraints of quasi-equilibrium, as outlined in Eqs. 9 and 10. Within these equations, the diffusion coefficient is symbolized by D^{ij}_{α}, the phase concentration is c^{j}_{α}, and the chemical mobility coefficient is M^{ij}.

$$\dot{c}^{i}(\vec{x}, t) = \nabla\sum_{j=1}^{n-1} M^{ij}(\{\phi_\alpha\}, \vec{c})\nabla\tilde{\mu}^{j} \tag{9}$$

$$\dot{c}^{i} = \nabla\sum_{\alpha=1}^{\nu}\sum_{j=1}^{n-1}\phi_\alpha D^{ij}_{\alpha}\nabla c^{j}_{\alpha} \quad with \quad D^{ij}_{\alpha} = \sum_{l=1}^{n-1} M^{il}_{\alpha}\Phi^{lj}_{\alpha} \tag{10}$$

The model is embraced by the incorporation of two supplementary parameters, $A_{\alpha\beta}$ and $J_{\alpha\beta\gamma}$. These parameters account for the anisotropic interfacial influence and the higher-order forces arising from multiple junctions, respectively. Furthermore, the values of $\Delta G_{\alpha\beta}$ and D_α are determined via TQ-coupling within the Thermo-Calc software [20], utilizing the TCFE10 and MOBFE4 databases to access thermodynamic and mobility information. Lastly, the solution to these equations is achieved through a finite-difference method.

$$A_{\alpha\beta} = -\frac{\nabla a^{\sigma}_{\alpha\beta}}{a^{\sigma}_{\alpha\beta}}(\nabla\phi_\beta - \nabla\phi_\alpha) \quad interfacial \quad anisotropy \quad term + \frac{1}{a^{\sigma}_{\alpha\beta}}\sum_{i=1}^{3}\nabla_i\left[\left(\frac{\partial a^{\sigma}_{\alpha\beta}}{\partial\nabla_i\phi_\beta} - \frac{\partial a^{\sigma}_{\alpha\beta}}{\partial\nabla_i\phi_\alpha}\right)\left(\frac{\pi^2}{2\eta^2}\phi_\alpha\phi_\beta - \frac{1}{2}\nabla\phi_\alpha\nabla\phi_\beta\right)\right]$$

$$J_{\alpha\beta\gamma} = \frac{1}{2}(\sigma_{\beta\gamma} - \sigma_{\alpha\gamma})\left(\frac{\pi^2}{\eta^2}\phi_\gamma + \nabla^2\phi_\gamma\right) \quad higher \quad order \quad junction \quad forces \tag{11}$$

Appendix B. Supporting information

Supplementary data associated with this article can be found in the online version at doi:10.1016/j.addma.2023.103859.

References

[1] T. DebRoy, T. Mukherjee, J.O. Milewski, J.W. Elmer, B. Ribic, J.J. Blecher, W. Zhang, Scientific, technological and economic issues in metal printing and their solutions, Nat. Mater. 18 (2019) 1026–1032, https://doi.org/10.1038/s41563-019-0408-2.

[2] M.V. Pantawane, Y.-H. Ho, S.S. Joshi, N.B. Dahotre, Computational assessment of thermokinetics and associated microstructural evolution in laser powder bed fusion manufacturing of Ti6Al4V alloy, Sci. Rep. 10 (2020), 7579, https://doi.org/10.1038/s41598-020-63281-4.

[3] Y. Li, D. Gu, Parametric analysis of thermal behavior during selective laser melting additive manufacturing of aluminum alloy powder, Mater. Des. 63 (2014) 856–867, https://doi.org/10.1016/j.matdes.2014.07.006.

[4] S.A. Khairallah, A.T. Anderson, A. Rubenchik, W.E. King, Laser powder-bed fusion additive manufacturing: physics of complex melt flow and formation mechanisms of pores, spatter, and denudation zones, Acta Mater. 108 (2016) 36–45, https://doi.org/10.1016/j.actamat.2016.02.014.

[5] T. DebRoy, H.L. Wei, J.S. Zuback, T. Mukherjee, J.W. Elmer, J.O. Milewski, A. M. Beese, A. Wilson-Heid, A. De, W. Zhang, Additive manufacturing of metallic components – process, structure and properties, Prog. Mater. Sci. 92 (2018) 112–224, https://doi.org/10.1016/j.pmatsci.2017.10.001.

[6] W.J. Sames, F.A. List, S. Pannala, R.R. Dehoff, S.S. Babu, The metallurgy and processing science of metal additive manufacturing, Int. Mater. Rev. 61 (2016) 315–360, https://doi.org/10.1080/09506608.2015.1116649.

[7] P.C. Collins, D.A. Brice, P. Samimi, I. Ghamarian, H.L. Fraser, Microstructural control of additively manufactured metallic materials, Annu. Rev. Mater. Res. 46 (2016) 63–91, https://doi.org/10.1146/annurev-matsci-070115-031816.

[8] Y.M. Wang, T. Voisin, J.T. McKeown, J. Ye, N.P. Calta, Z. Li, Z. Zeng, Y. Zhang, W. Chen, T.T. Roehling, R.T. Ott, M.K. Santala, P.J. Depond, M.J. Matthews, A. V. Hamza, T. Zhu, Additively manufactured hierarchical stainless steels with high strength and ductility, Nat. Mater. 17 (2018) 63–71, https://doi.org/10.1038/nmat5021.

[9] D. Herzog, V. Seyda, E. Wycisk, C. Emmelmann, Additive manufacturing of metals, Acta Mater. 117 (2016) 371–392, https://doi.org/10.1016/j.actamat.2016.07.019.

[10] W.E. Frazier, Metal additive manufacturing: a review, J. Mater. Eng. Perform. 23 (2014) 1917–1928, https://doi.org/10.1007/s11665-014-0958-z.

[11] D.D. Gu, W. Meiners, K. Wissenbach, R. Poprawe, Laser additive manufacturing of metallic components: materials, processes and mechanisms, Int. Mater. Rev. 57 (2012) 133–164, https://doi.org/10.1179/1743280411Y.0000000014.

[12] D. Zhang, S. Sun, D. Qiu, M.A. Gibson, M.S. Dargusch, M. Brandt, M. Qian, M. Easton, Metal alloys for fusion-based additive manufacturing, Adv. Eng. Mater. 20 (2018), 1700952, https://doi.org/10.1002/adem.201700952.
[13] ASM International Handbook Committee., Properties and Selection: Irons, Steels, and High-Performance Alloys.
[14] R. Kuziak, R. Kawalla, S. Waengler, Advanced high strength steels for automotive industry, Arch. Civ. Mech. Eng. 8 (2008) 103–117, https://doi.org/10.1016/S1644-9665(12)60197-6.
[15] G. Sweet, I.W. Donaldson, C.T. Schade, M.Y. Amegadzie, D.P. Bishop, Laser free-form fabrication of dual phase DP600 steel using water atomized feedstock powder, Addit. Manuf. 47 (2021), 102357, https://doi.org/10.1016/j.addma.2021.102357.
[16] J. Dilip, G.J. Ram, T.L. Starr, B. Stucker, Selective laser melting of HY100 steel: process parameters, microstructure and mechanical properties, Addit. Manuf. 13 (2017) 49–60, https://doi.org/10.1016/j.addma.2016.11.003.
[17] R. Seede, D. Shoukr, B. Zhang, A. Whitt, S. Gibbons, P. Flater, A. Elwany, R. Arroyave, I. Karaman, An ultra-high strength martensitic steel fabricated using selective laser melting additive manufacturing: Densification, microstructure, and mechanical properties, Acta Mater. 186 (2020) 199–214, https://doi.org/10.1016/j.actamat.2019.12.037.
[18] R. Seede, B. Zhang, A. Whitt, S. Picak, S. Gibbons, P. Flater, A. Elwany, R. Arroyave, I. Karaman, Effect of heat treatments on the microstructure and mechanical properties of an ultra-high strength martensitic steel fabricated via laser powder bed fusion additive manufacturing, Addit. Manuf. 47 (2021), 102255, https://doi.org/10.1016/j.addma.2021.102255.
[19] C.A. Schneider, W.S. Rasband, K.W. Eliceiri, NIH Image to ImageJ: 25 years of image analysis, Nat. Methods 9 (2012) 671–675, https://doi.org/10.1038/nmeth.2089.
[20] J.O. Andersson, Thomas Helander, Lars Höglund, Pingfang Shi, Bo Sundman, Thermo-Calc & DICTRA, computational tools for materials science, Calphad 26 (2002) 273–312, https://doi.org/10.1016/S0364-5916(02)00037-8.
[21] G. Nolze, R. Hielscher, Orientations – perfectly colored, J. Appl. Crystallogr 49 (2016) 1786–1802, https://doi.org/10.1107/S1600576716012942.
[22] F. Bachmann, R. Hielscher, H. Schaeben, Grain detection from 2d and 3d EBSD data–specification of the MTEX algorithm, Ultramicroscopy 111 (2011) 1720–1733, https://doi.org/10.1016/j.ultramic.2011.08.002.
[23] F. Bachmann, R. Hielscher, H. Schaeben, Texture analysis with MTEX – free and open source software toolbox, SSP 160 (2010) 63–68, https://doi.org/10.4028/www.scientific.net/SSP.160.63.
[24] F. Niessen, T. Nyyssönen, A.A. Gazder, R. Hielscher, Parent grain reconstruction from partially or fully transformed microstructures in MTEX, J. Appl. Crystallogr 55 (2022) 180–194, https://doi.org/10.1107/S1600576721011560.
[25] B. Böttger, J. Eiken, M. Apel, Multi-ternary extrapolation scheme for efficient coupling of thermodynamic data to a multi-phase-field model, Comput. Mater. Sci. 108 (2015) 283–292, https://doi.org/10.1016/j.commatsci.2015.03.003.
[26] J. Eiken, B. Böttger, I. Steinbach, Multiphase-field approach for multicomponent alloys with extrapolation scheme for numerical application, Phys. Rev. E Stat. Nonlin. Soft Matter Phys. 73 (2006) 66122, https://doi.org/10.1103/PhysRevE.73.066122.
[27] G. Boussinot, M. Döring, S. Hemes, O. Stryzhyboroda, M. Apel, M. Schmidt, Laser powder bed fusion of eutectic Al–Ni alloys: experimental and phase-field studies, Mater. Des. 198 (2021), 109299, https://doi.org/10.1016/j.matdes.2020.109299.
[28] G. Boussinot, M. Apel, J. Zielinski, U. Hecht, J.H. Schleifenbaum, Strongly out-of-equilibrium columnar solidification during laser powder-bed fusion in additive manufacturing, Phys. Rev. Appl. 11 (2019), https://doi.org/10.1103/PhysRevApplied.11.014025.
[29] V.P. Narayana Samy, M. Schäfle, F. Brasche, U. Krupp, C. Haase, Understanding the mechanism of columnar–to-equiaxed transition and grain refinement in additively manufactured steel during laser powder bed fusion, Addit. Manuf. 73 (2023), 103702, https://doi.org/10.1016/j.addma.2023.103702.
[30] P. Köhnen, M. Létang, M. Voshage, J.H. Schleifenbaum, C. Haase, Understanding the process-microstructure correlations for tailoring the mechanical properties of L-PBF produced austenitic advanced high strength steel, Addit. Manuf. 30 (2019), 100914, https://doi.org/10.1016/j.addma.2019.100914.
[31] W. Pantleon, Resolving the geometrically necessary dislocation content by conventional electron backscattering diffraction, Scr. Mater. 58 (2008) 994–997, https://doi.org/10.1016/j.scriptamat.2008.01.050.
[32] M. Ohno, K. Matsuura, Quantitative phase-field modeling for two-phase solidification process involving diffusion in the solid, Acta Mater. 58 (2010) 5749–5758, https://doi.org/10.1016/j.actamat.2010.06.050.
[33] J. Liu, J. Yanagimoto, Ferrite nucleation kinetics inside austenite grain, ISIJ Int. 47 (2007) 1188–1194, https://doi.org/10.2355/isijinternational.47.1188.
[34] A. Carré, B. Böttger, M. Apel, Implementation of an antitrapping current for a multicomponent multiphase-field ansatz, J. Cryst. Growth 380 (2013) 5–13, https://doi.org/10.1016/j.jcrysgro.2013.05.032.
[35] C. Wei, J. Zhang, S. Yang, W. Tao, F. Wu, W. Xia, Experiment-based regional characterization of HAZ mechanical properties for laser welding, Int. J. Adv. Manuf. Technol. 78 (2015) 1629–1640, https://doi.org/10.1007/s00170-014-6762-y.
[36] A. Ramazani, K. Mukherjee, A. Abdurakhmanov, M. Abbasi, U. Prahl, Characterization of microstructure and mechanical properties of resistance spot welded DP600 steel, Metals 5 (2015) 1704–1716, https://doi.org/10.3390/met5031704.
[37] J. Gould, S. Khurana, T. Li, Predictions of microstructures when welding automotive advanced high-strength steels, Weld. J. 85 (2006) 111s–116s.
[38] W. Hearn, K. Lindgren, J. Persson, E. Hryha, In situ tempering of martensite during laser powder bed fusion of Fe-0.45C steel, Materialia 23 (2022), 101459, https://doi.org/10.1016/j.mtla.2022.101459.
[39] S. Kou. Welding metallurgy, 2nd ed.,, John Wiley & Sons, Hoboken, NJ, 2003.
[40] F. Yan, W. Xiong, E. Faierson, G.B. Olson, Characterization of nano-scale oxides in austenitic stainless steel processed by powder bed fusion, Scr. Mater. 155 (2018) 104–108, https://doi.org/10.1016/j.scriptamat.2018.06.011.
[41] J.-Y. Kang, S.-J. Park, M.-B. Moon, Phase analysis on dual-phase steel using band slope of electron backscatter diffraction pattern, Microsc. Microanal. 19 (Suppl 5) (2013) 13–16, https://doi.org/10.1017/S1431927613012233.
[42] George Krauss, Martensite in steel: strength and structure, Mater. Sci. Eng.: A 273–275 (1999) 40–57, https://doi.org/10.1016/S0921-5093(99)00288-9.
[43] H. Pirgazi, M. Sanjari, S. Tamimi, B. Shalchi Amirkhiz, L.A.I. Kestens, M. Mohammadi, Texture evolution in selective laser melted maraging stainless steel CX with martensitic transformation, J. Mater. Sci. 56 (2021) 844–853, https://doi.org/10.1007/s10853-020-05290-2.
[44] S.A.H. Motaman, C. Haase, The microstructural effects on the mechanical response of polycrystals: a comparative experimental-numerical study on conventionally and additively manufactured metallic materials, Int. J. Plast. 140 (2021), 102941, https://doi.org/10.1016/j.ijplas.2021.102941.
[45] S.A.H. Motaman, F. Roters, C. Haase, Anisotropic polycrystal plasticity due to microstructural heterogeneity: a multi-scale experimental and numerical study on additively manufactured metallic materials, Acta Mater. 185 (2020) 340–369, https://doi.org/10.1016/j.actamat.2019.12.003.
[46] H.K.D.H. Bhadeshia, L.-E. Svensson, B. Gretoft, The austenite grain structure of low-alloy steel weld deposits, J. Mater. Sci. 21 (1986) 3947–3951, https://doi.org/10.1007/BF02431634.
[47] K. Mundra, T. Debroy, S. Babu, S. David, Weld metal microstructure calculations from fundamentals of transport phenomena in the Arc welding of low-alloy steels, Weld. J. (76) (1997).
[48] N.S. POttore, C.I. Garcia, A.J. DeArdo, Interrupted and isothermal solidification studies of low and medium carbon steels, MTA 22 (1991) 1871–1880, https://doi.org/10.1007/BF02646512.
[49] D. Phelan, R. Dippenaar, Instability of the delta-ferrite/austenite interface in low carbon steels: the influence of delta-ferrite recovery sub-structures, ISIJ Int. 44 (2004) 414–421, https://doi.org/10.2355/isijinternational.44.414.
[50] H. Yin, T. Emi, H. Shibata, Morphological instability ofδ-ferrite/γ-austenite interphase boundary in low carbon steels, Acta Mater. 47 (1999) 1523–1535, https://doi.org/10.1016/S1359-6454(99)00022-1.
[51] T. Shinozaki, Y. Tomota, T. Fukino, T. Suzuki, Microstructure evolution during reverse transformation of austenite from tempered martensite in low alloy steel, ISIJ Int. 57 (2017) 533–539, https://doi.org/10.2355/isijinternational.ISIJINT-2016-557.
[52] M. Tokizane, N. Matsumura, K. Tsuzaki, T. MAKI, I. Tamura, Recrystallization and formation of austenite in deformed lath martensitic structure of low carbon steels, Met. Mat. Trans. A 13 (1982) 1379–1388, https://doi.org/10.1007/BF02642875.
[53] B. Krebs, L. Germain, A. Hazotte, M. Gouné, Banded structure in Dual Phase steels in relation with the austenite-to-ferrite transformation mechanisms, J. Mater. Sci. 46 (2011) 7026–7038, https://doi.org/10.1007/s10853-011-5671-9.
[54] G. KRAUSS, Solidification, segregation, and banding in carbon and alloy steels, Metall. Mater. Trans. B 34 (2003) 781–792, https://doi.org/10.1007/s11663-003-0084-z.
[55] M. Daamen, C. Haase, J. Dierdorf, D.A. Molodov, G. Hirt, Twin-roll strip casting: a competitive alternative for the production of high-manganese steels with advanced mechanical properties, Mater. Sci. Eng.: A 627 (2015) 72–81, https://doi.org/10.1016/j.msea.2014.12.069.
[56] R.A. Grange, Effect of microstructural banding in steel, Metall. Trans. 2 (1971) 417–426, https://doi.org/10.1007/BF02663328.
[57] N. Fonstein, Dual-phase steels, in: Automotive Steels, Elsevier, 2017, pp. 169–216.
[58] T.F. Majka, D.K. Matlock, G. KRAUSS, Development of microstructural banding in low-alloy steel with simulated Mn segregation, Metall. Mater. Trans. A 33 (2002) 1627–1637, https://doi.org/10.1007/s11661-002-0172-8.
[59] Y. Chang, M. Lin, U. Hangen, S. Richter, C. Haase, W. Bleck, Revealing the relation between microstructural heterogeneities and local mechanical properties of complex-phase steel by correlative electron microscopy and nanoindentation characterization, Mater. Des. 203 (2021), 109620, https://doi.org/10.1016/j.matdes.2021.109620.
[60] Y. Chang, C. Haase, D. Szeliga, L. Madej, U. Hangen, M. Pietrzyk, W. Bleck, Compositional heterogeneity in multiphase steels: characterization and influence on local properties, Mater. Sci. Eng.: A 827 (2021), 142078, https://doi.org/10.1016/j.msea.2021.142078.
[61] D. Raabe, S. Sandlöbes, J. Millán, D. Ponge, H. Assadi, M. Herbig, P.-P. Choi, Segregation engineering enables nanoscale martensite to austenite phase transformation at grain boundaries: a pathway to ductile martensite, Acta Mater. 61 (2013) 6132–6152, https://doi.org/10.1016/j.actamat.2013.06.055.
[62] J. Hu, L.X. Du, H. Liu, G.S. Sun, H. Xie, H.L. Yi, R. Misra, Structure–mechanical property relationship in a low-C medium-Mn ultrahigh strength heavy plate steel with austenite-martensite submicro-laminate structure, Mater. Sci. Eng.: A 647 (2015) 144–151, https://doi.org/10.1016/j.msea.2015.09.008.
[63] F.H. Samuel, Effect of dual-phase treatment and tempering on the microstructure and mechanical properties of a high strength, low alloy steel, Mater. Sci. Eng. 75 (1985) 51–66, https://doi.org/10.1016/0025-5416(85)90177-6.
[64] C.C. Tasan, M. Diehl, D. Yan, M. Bechtold, F. Roters, L. Schemmann, C. Zheng, N. Peranio, D. Ponge, M. Koyama, K. Tsuzaki, D. Raabe, An overview of dual-phase steels: advances in microstructure-oriented processing and micromechanically

guided design, Annu. Rev. Mater. Res. 45 (2015) 391–431, https://doi.org/10.1146/annurev-matsci-070214-021103.
[65] H. Ashrafi, M. Shamanian, R. Emadi, N. Saeidi, Correlation of tensile properties and strain hardening behavior with martensite volume fraction in dual-phase steels, Trans. Indian Inst. Met. 70 (2017) 1575–1584, https://doi.org/10.1007/s12666-016-0955-z.
[66] A.-P. Pierman, O. Bouaziz, T. Pardoen, P.J. Jacques, L. Brassart, The influence of microstructure and composition on the plastic behaviour of dual-phase steels, Acta Mater. 73 (2014) 298–311, https://doi.org/10.1016/j.actamat.2014.04.015.
[67] C.C. Tasan, J. Hoefnagels, M. Diehl, D. Yan, F. Roters, D. Raabe, Strain localization and damage in dual phase steels investigated by coupled in-situ deformation experiments and crystal plasticity simulations, Int. J. Plast. 63 (2014) 198–210, https://doi.org/10.1016/j.ijplas.2014.06.004.
[68] J.R. Croteau, S. Griffiths, M.D. Rossell, C. Leinenbach, C. Kenel, V. Jansen, D. N. Seidman, D.C. Dunand, N.Q. Vo, Microstructure and mechanical properties of Al-Mg-Zr alloys processed by selective laser melting, Acta Mater. 153 (2018) 35–44, https://doi.org/10.1016/j.actamat.2018.04.053.
[69] S. Thapliyal, S. Shukla, Le Zhou, H. Hyer, P. Agrawal, P. Agrawal, M. Komarasamy, Y. Sohn, R.S. Mishra, Design of heterogeneous structured Al alloys with wide processing window for laser-powder bed fusion additive manufacturing, Addit. Manuf. 42 (2021), 102002, https://doi.org/10.1016/j.addma.2021.102002.